RESEARCH ARTICLE | MARCH 27 2025

A logic gate based on photonic structure of liquid crystal and the theoretical design of dual polarization multi-physical quantity detection

Na Pei (裴娜); Li-Jie Huang (黄礼杰) ; Hai-Feng Zhang (章海锋)

Physics of Fluids 37, 037201 (2025)
https://doi.org/10.1063/5.0259661

Physics of Fluids ARTICLE pubs.aip.org/aip/pof

A logic gate based on photonic structure of liquid crystal and the theoretical design of dual polarization multi-physical quantity detection

Cite as: Phys. Fluids **37**, 037201 (2025); doi: 10.1063/5.0259661
Submitted: 20 January 2025 · Accepted: 7 March 2025 ·
Published Online: 27 March 2025

View Online Export Citation CrossMark

Na Pei (裴娜),[1] Li-Jie Huang (黄礼杰),[2] and Hai-Feng Zhang (章海锋)[2,a)]

AFFILIATIONS

[1]School of Integrated Circuit Science and Engineering, Nanjing University of Posts and Telecommunications, Nanjing 210023, China
[2]College of Electronic and Optical Engineering and College of Flexible Electronics (Future Technology), Nanjing University of Posts and Telecommunications, Nanjing 210023, China

[a)]Author to whom correspondence should be addressed: hanlor@163.com and hanlor@njupt.edu.cn

ABSTRACT

In this paper, a multifunctional layered photonic structure capable of implementing various logic gates and detecting multiple physical quantities is proposed. This structure is achieved through the arrangement of various dielectrics with the incorporation of anisotropic plasmas and liquid crystal materials, imparting tunability and multiscale characteristics. Meanwhile, sharp transmission peaks (TPs) can be obtained, which follows the rule of NOR ("NOT OR" gate) logic and AND ("AND" gate) logic gates for transverse magnetic and transverse electric polarization by judging the values of TPs. By locking the frequency point at the TP, simultaneous sensing of the refractive index, the angle between the incident wave and electric field, magnetic field strength, and temperature can be achieved. Various parameters for evaluating sensing performance have also been introduced, and their respective sensitivities within normalized frequency (2πc/dare obtained as follows: 8.75×10^{-4} (2πc/d)/RIU or 2.5×10^{-4} (2πc/d)/RIU, 1.7×10^{-3} (2πc/d)/T or 2×10^{-3} (2πc/d)/T, 0.0882 (2πc/d)/° or 0.0957 (2πc/d)/°, 4.87×10^{-4} (2πc/d)/K or 7.22×10^{-4} (2πc/d)/K. Unlike conventional sensors, this device has the capability of tunable logic gates and multi-physics quantity detection, which has a wide range of application scenarios in light computing and biosensing fields.

I. INTRODUCTION

In recent years, multifunctional layered photonic structure (MLPS)[1] has appeared in various research fields, such as optics,[2,3] photonics,[4,5] and electromagnetic fields.[6] The MLPS is a structure composed of layered materials with different refractive media, which can create photonic band gaps[7,8] (PBGs) where electromagnetic waves (EWs) cannot propagate. When a defect layer is introduced, the interference behavior of EWs is modified so that EWs of a particular frequency can pass through, enabling the regulation of EWs. Furthermore, by introducing anisotropic plasma and liquid crystal materials, the MLPS exhibits distinct transmittances for transverse electric (TE) and transverse magnetic (TM) polarization,[9] which can be tuned through external factors such as magnetic field and temperature. Taking advantage of these features, MLPS has important applications in the field of logic gates,[10] fibers,[11,12] filters,[13] waveguides,[14] and sensors.[15,16]

Like the evolution of sensors, logic gates, as crucial components of integrated circuits, have also undergone a transformative journey, transitioning from individual entities to integrated gates. Pirzadi *et al.*[17] proposed a precise all-optical OR logic gate through the unique combination of single-line defect, Mach–Zehnder interferometer, and ring resonator. This logic gate exhibits the capability for dense integration and can be applied in high-precision photonic integrated circuits. Veisi *et al.*[18] designed an all-optical AND logic gate based on the Kerr effect, utilizing a photonic crystal ring resonator structure. Mohebzadeh-Bahabady and Olyaee[19] proposed a photonic crystals nanoresonator structure based on interference effects, composed of three waveguides and a nanoscale resonator, which can simultaneously achieve all-optical NOT and XOR logic gates. However, these logic gates are limited to singular functionalities and cannot simultaneously achieve both logic gate operations and the detection of multiple physical quantities. Therefore, the integration of tunable logic gates with

multi-function sensors becomes significant. This integration allows for the handling of diverse relationships between various physical quantities through different logic operations, while simultaneously enabling the acquisition of extensive information through multi-physical quantity sensing. The integration of logic gates and multisensor-equipped MLPS presents extensive application scenarios, facilitating comprehensive research in areas such as industrial automation,[20,21] medical monitoring,[22] and transportation.[23]

With the relentless progress and iterative advancements in sensor technology, it has emerged as a pivotal focal point in the realm of scientific research. Ge *et al.*[24] developed a magnetic sensor based on one-dimensional photonic crystals, achieving a sensitivity (S) of 0.817 nm/Oe and a figure of merit (FOM) of $17.439\,\mathrm{O} \times 10^{-1}$. This was accomplished by employing strictly coupled waves to analyze the refractive index variation of a magnetohydrodynamic thin film in response to a magnetic field. In a separate study, Baraket *et al.*[25] designed a nonlinear temperature-tunable filter using one-dimensional superconductor photonic crystals, leveraging thermal expansion and thermo-optical effects. Zaky *et al.*[26] devised a gas sensor by placing a gas chamber between one-dimensional porous silicon photonic crystals and a silver layer deposited on a prism. This design achieved a remarkable S of 1.9×10^5 nm/RIU and a low detection limit (DL) of 1.4×10^{-7} RIU. However, Stern *et al.*[27] explored multi-physical quantity sensors prompted by the limitation of single-physical-quantity sensing in daily measurements. They developed a sensor capable of simultaneously measuring temperature and refractive index (RI) with a high S,[27] enabling the acquisition of more comprehensive and accurate information by integrating multiple sensing functions.

In this paper, a MLPS based on magnetized plasma material and liquid crystal has been developed. It can function as NOR ("NOT OR" gate) and AND ("AND" gate) logic gates under TM and TE polarization, respectively. Simultaneously, while meeting the requirements of logic gates, it possesses the capability for detecting multiple physical quantities. The MLPS can be constructed by adjusting the arrangement of layered media and introducing anisotropic materials. After introducing plasma and liquid crystal materials as defect layers into the structure, a localized defect mode resonance[28,29] (LDMR) is generated, resulting in a sharp transmission peak (TP). Since the RI of liquid crystal is affected not only by temperature but also by the angle between the incident wave and electric field (ABIE),[30] tuning of the MLPS can be achieved by adjusting ABIE and temperature. Additionally, as both liquid crystal[31] and plasma[32] belong to anisotropic media, they exhibit different refractive dielectrics under TM and TE conditions. Based on this, we can implement both AND and NOR logic gates by detecting the peak value of TP. When the TP value exceeds 0.9, it is determined that TP is present. Furthermore, when the relevant physical quantities of the MLPS change, the resonance frequency of TP also changes accordingly. Therefore, the functionality of detecting multiple physical quantities can be achieved by fitting the linear relationship between RI, magnetic fields, ABIE, temperature, and the movement of the frequency point (FP). The results exhibit strong linearity, a high FOM, and a high quality factor (Q), while still adhering to the logic gate relationships. MLPS, possessing not only two types of logic gates but also the capability for detecting multiple physical quantities, enables the comprehensive integration of more extensive information. MLPS allows for advanced data analysis, simultaneously reducing costs and optimizing resource utilization, which holds significant research significance and potential.

II. STRUCTURE AND PRINCIPLE OF OPERATION

The MLPS depicted in Fig. 1 can be fabricated through the process of etching.[33] The fabrication procedure for the MLPS can be seen in Sec. I of the supplementary material. The RI of dielectrics A and B is $n_A = 2.76$ and $n_B = 2.35$, respectively. The valuable contributions of Lewin[34] in deriving expressions for the effective permittivity and permeability of composites allowed us to achieve the desired RI within a specific range. Layer D is the nanocomposite material, which is composed of Ag nanoparticles embedded in host material SiO_2,[32] and the RI and thickness are denoted by n_D and d_D. To provide a more accurate description of the thickness of each media, this paper employs the concept of normalized thickness d_0, which is set at a value of 140 mm. Also, depending on the normalized thickness, the angular frequency of the electromagnetic wave can be normalized to $\omega_0 = 2\pi c/d_0$, denoted by α. In this structure, the thicknesses of the two dielectrics A and B are $d_A = 0.3d_0$ and $d_B = 0.3d_0$. The thickness of layer D is $d_D = 0.2d_0$. The thicknesses of the chosen defect layers, consisting of one liquid

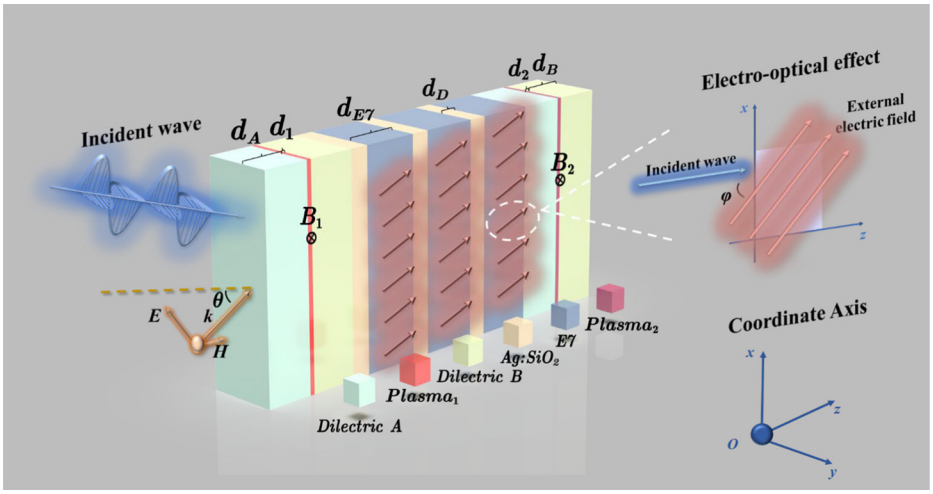

FIG. 1. The asymmetric MLPS comprises media filled with various colors, plasma, and liquid crystal. EWs enter from positive direction (+z axis) at angles denoted by θ. The ABIE is denoted by φ. The direction of the magnetic field B_1 and B_2 is designated with the coordinate axis as a reference.

crystal and two plasma layers, are $d_{E7} = 2d_0$, $d_1 = 0.022d_0$, and $d_2 = 0.022d_0$. With both fields oriented parallel to the $+y$ axis, the external magnetic fields, denoted as B_1 and B_2, are applied to plasma1 and plasma2, respectively, with initial values $B_1 = 1.5$ T, $B_2 = 1.7$ T. Xuan *et al.*[35] developed a method to generate a spatial linear magnetic field by applying a linear current. Hence, a linearly controllable magnetic field can be spatially generated to satisfy the different precise requirements of the magnetic field in the two plasma media. Additionally, because of the spatial separation between plasma1 and plasma2, magnetic fields corresponding to the two are unlikely to interfere. EWs are incident from positive directions along the $+z$ axis at 0°, the initial ABIE and the temperature are $\varphi = 30°$ and $T_0 = 293.15$ K, which are used to control electro-optic effects[36] in liquid crystal.

The dielectric tensor function of plasma anisotropy can be expressed as follows:[32]

$$\varepsilon_{\text{Plasma}} = \begin{pmatrix} \varepsilon_1 & 0 & i\varepsilon_2 \\ 0 & \varepsilon_3 & 0 \\ -i\varepsilon_2 & 0 & \varepsilon_1 \end{pmatrix}. \tag{1}$$

Each of these tensors can be expressed as follows:[32]

$$\varepsilon_1 = 1 - \frac{\omega_p^2(\omega + i\nu_c)}{\omega[(\omega + i\nu_c)^2 - \omega_c^2]}, \tag{2}$$

$$\varepsilon_2 = -\frac{i\omega_p^2\omega_c}{\omega[(\omega + i\nu_c)^2 - \omega_c^2]}, \tag{3}$$

$$\varepsilon_3 = 1 - \frac{\omega_p^2}{\omega(\omega + i\nu_c)}, \tag{4}$$

where $\omega_c = (eB_0/m)$ is the electron cyclotron frequency, $\omega_p = (e^2 n_e/\varepsilon_0 m)^{1/2}$ is the plasma frequency, n_e is the plasma density, and ν_c is the collision frequency. In this paper, the values are as follows:[32] $\omega_c = eB/m$, $\upsilon_c = 0.001\omega_p$, $n_e = 1.1 \times 10^{19}$ m^{-3}, $e = 1.6 \times 10^{-19}$ C, $m = 9.1 \times 10^{-31}$ kg, and $\varepsilon_0 = 8.8542 \times 10^{-12}$ F/m. When an external magnetic field is applied, the propagation of EWs in the plasma is affected by the Lorentz force due to TM polarization.[32] For TE polarization, the plasma in the MLPS controlled by the external magnetic fields B_1 and B_2 will exhibit the same features as in the absence of the external field. In this paper, we give the overall performance of the MLPS under TM and TE polarization and analyze the entire structure using the transmission matrix method. First, we express the relative permittivity of plasma under TM and TE polarization as follows:[32]

$$\varepsilon_{\text{TM}} = \frac{\varepsilon_1^2 - \varepsilon_2^2}{\varepsilon_1}, \tag{5}$$

$$\varepsilon_{\text{TE}} = \varepsilon_3. \tag{6}$$

Subsequently, the refractive indices of the two plasmas can be derived from $n_{TM} = \sqrt{\varepsilon_{\text{TM}}}$, and their transmission matrices can be expressed in the following form:[32]

$$\mathbf{M}_k = \begin{pmatrix} \cos(k_{kz}d_k) + \dfrac{k_{kx}c_{xz}}{k_{kx}c_x}\sin(k_{kz}d_k) & -\dfrac{i}{\eta_k}\left[1 + \left(\dfrac{k_{kx}c_{xz}}{k_{kx}c_x}\right)^2\right]\sin(k_{kz}d_k) \\ -i\eta_k \sin(k_{kz}d_k) & \cos(k_{kz}d_k) - \dfrac{k_{kx}c_{xz}}{k_{kx}c_x}\sin(k_{kz}d_k) \end{pmatrix}, \tag{7}$$

where the constituents of the wave along the $+x$ and $+z$ axes, k_{kx} and k_{kz}, represent the conductivity of light, c and u_0 symbolize the velocity of light $c = 3 \times 10^8$ m/s and the permeability $\mu_0 = 4\pi \times 10^{-7}$ N m^{-1}.

For ordinary dielectrics, the transmission matrix can be written as[32]

$$\mathbf{M}_j = \begin{pmatrix} \cos(k_{jz}d_j) & -\dfrac{i}{\eta_j}\sin(k_{jz}d_j) \\ -i\eta_j \sin(k_{jz}d_j) & \cos(k_{jz}d_j) \end{pmatrix}, \tag{8}$$

where, $k_{jz} = n_j w/c \cos\theta_j$ is also the component of the wave in the z axis, d_j is the thickness of the dielectric, j donated by A, B, and D, representing three common dielectrics.

In the context of liquid crystal media, the orientation and spatial distribution of nematic liquid crystal molecules are affected by an applied field. This results in an alteration of the optical properties and the generation of electro-optic effects.[37,38] When the magnitude of the applied electric field exceeds a certain threshold, the nematic liquid crystal molecules align parallel to the direction of the electric field.[39] Under these conditions, the nematic liquid crystal can be treated as a dielectric material characterized by a single dielectric axis. Its effective RI can be mathematically expressed as follows:[39]

$$n_{\text{eff}} = \frac{n_o n_e}{\sqrt{n_o^2 \cos^2\varphi + n_e^2 \sin^2\varphi}}, \tag{9}$$

$$n_e(T_0) = A + BT_0 + \frac{2(\Delta n)_0}{3}\left(1 - \frac{T_0}{T_c}\right)^{\beta}, \tag{10}$$

$$n_o(T_0) = A + BT_0 - \frac{(\Delta n)_0}{3}\left(1 - \frac{T_0}{T_c}\right)^{\beta}, \tag{11}$$

where n_o and n_e represent the RI of ordinary light and extraordinary light, respectively, φ represents the angle between the applied electric field and the direction of the normal incident wave. The electric field applied to the sample is generated utilizing inclined electrode plates, which can be seen in Sec. IV of the supplementary material. $(\Delta n)_0$ represents the nematic liquid crystal birefringence corresponding to the temperature $T_0 = 0$ K, T_c represents the critical temperature at which the nematic phase of the liquid crystal transforms into an isotropic phase, and A and B are the liquid crystal material constants.

According to the material properties of 2-cyano-4-pentylpheny4-(4-heptylcyclohexyl) benzoate nematic liquid crystal,[39] the relevant parameters can be obtained as follows:[39] $A = 1.6493$, $B = -3.66 \times 10^{-4}$, $(\Delta n)_0 = 0.178$, and $\beta = 0.2518$.

For the nano-composite layer D, we employ the effective medium approximation method to describe its optical properties. This approach assumes that a non-uniform mixture of different materials with macroscopic optical uniformity can be characterized by a certain effective relative dielectric constant ε_D,[40]

$$\frac{\varepsilon_D - \varepsilon_m}{2\varepsilon_m + \varepsilon_D} = \eta \frac{\varepsilon_p - \varepsilon_m}{2\varepsilon_m + \varepsilon_p}, \tag{12}$$

where η is the volume fraction of inclusions; ε_m and ε_p are the dielectric permittivities of the matrix and inclusions, respectively.

To describe the optical properties of metal nanoparticles, the model of Drude is used as follows:[41]

$$\varepsilon_p(\omega) = \varepsilon_0 - \frac{\omega_p^2}{\omega^2 + i\omega\gamma}, \tag{13}$$

where ε_0 is the contribution of the lattice to the relative permittivity of metal, ω_p is the plasma frequency of the free electron gas in infinite volume, and γ is the relaxation rate.[41]

In this paper, we consider incorporating Ag as nanoscale metal particles and SiO_2 as the matrix for the composite medium with the initial $\eta = 0.01$ and the permittivity $\varepsilon_m = 2.25$ and $\varepsilon_0 = 5.0$. For silver, the relevant parameters are as follows:[42] $\hbar\omega_p = 9.2159$ ev, $\hbar\gamma = 0.0212$ ev.

The entire transfer matrix $\mathbf{M}_F$ in the positive direction can be written as

$$\mathbf{M}_F = (\mathbf{M}_a\mathbf{M}_a\mathbf{M}_1\mathbf{M}_b\mathbf{M}_b)(\mathbf{M}_d\mathbf{M}_{E7})^3(\mathbf{M}_b\mathbf{M}_b\mathbf{M}_2\mathbf{M}_a\mathbf{M}_a). \tag{14}$$

From the above transmission matrix, the reflection and transmission coefficients can be calculated as follows:[32]

$$r = \frac{(m_{11} + m_{12}\eta_{N+1})\eta_0 - (m_{11} + m_{12}\eta_{N+1})}{(m_{11} + m_{12}\eta_{N+1})\eta_0 + (m_{11} + m_{12}\eta_{N+1})}, \tag{15}$$

$$t = \frac{2\eta_0}{(m_{11} + m_{12}\eta_{N+1})\eta_0 + (m_{11} + m_{12}\eta_{N+1})}. \tag{16}$$

Since both sides of the MLPS are air layers, $\eta_{N+1} = \eta_0 = (\varepsilon_0/u_0)^{1/2}/\cos\theta$. The corresponding reflectivity (Re) and transmissivity (Tr) are given by[32]

$$Re = |r|^2, \tag{17}$$

$$Tr = |t|^2. \tag{18}$$

III. RESULTS AND DISCUSSION

The functions of the MLPS, including its logical gate operation and its capability for detecting multi-physics quantities, will be elucidated more comprehensively in Sec. III. The experimental setup for the MLPS can be seen in Sec. II of the supplementary material.

In this paper, the two input variables are the angle between this incident wave and the electric field (ABIE) and the temperature (T_0). Importantly, the output variable is the transmittance (Tr) of this incident wave through the structure, which is controlled by the two input variables. By the two input variables, under TM and TE polarization, the logic gate functionality of this MLPS can be NOR and AND, respectively, which is modulated by a single incident wave. The truth table for the two logic gates is provided in Table I.

TABLE I. The truth table of NOR and AND logic gates belongs to two different polarizations and the contents of parentheses indicate the present conditions of two inputs.

Logic gate	In_1	In_2	Out
NOR (TM polarization)	0 ($\varphi = 0°$)	0 ($T_0 = 293.15$ K)	1 ($Tr > 0.9$)
	0 ($\varphi = 0°$)	1 ($T_0 = 345$ K)	0 ($Tr < 0.1$)
	1 ($\varphi = 30°$)	0 ($T_0 = 293.15$ K)	0 ($Tr < 0.1$)
	1 ($\varphi = 30°$)	1 ($T_0 = 345$ K)	0 ($Tr < 0.1$)
AND (TE polarization)	0 ($\varphi = 0°$)	0 ($T_0 = 293.15$ K)	0 ($Tr < 0.1$)
	0 ($\varphi = 0°$)	1 ($T_0 = 345$ K)	0 ($Tr < 0.1$)
	1 ($\varphi = 30°$)	0 ($T_0 = 293.15$ K)	0 ($Tr < 0.1$)
	1 ($\varphi = 30°$)	1 ($T_0 = 345$ K)	1 ($Tr > 0.9$)

For brevity, the two input terminals are denoted as "In_1" and "In_2," while the output terminal is labeled "Out," where $\varphi = 30°$ and $\varphi = 0°$ denote logical levels 1 and 0, that is, "$In_1 = 1$" and "$In_1 = 0$," respectively. Likewise, the logical levels 1 and 0 for the other input, T_0, are achieved when $T_0 = 345$ and $T_0 = 293.15$ K, that is "$In_2 = 0$" and "$In_2 = 1$," respectively. The output of the two distinct logic gates is expressed through reflectivity: an output logic of "1" is observed when $Tr > 0.9$, while an output logic of "0" is observed when $Tr < 0.1$, that is "Out = 0" and "Out = 1" respectively. When the EWs are incident with TM polarization, as illustrated in Fig. 2(a), when the ABIE is controlled at 0° at $T_0 = 293.15$ K, that is, under the conditions of "$In_1 = 0$" and "$In_2 = 0$," a sharp TP will be generated at $f = 1.7345\alpha$ with

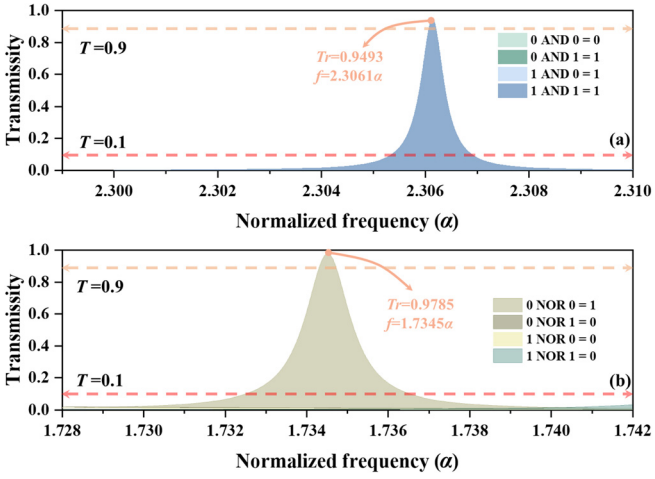

FIG. 2. Illustration of the transmission spectra generated through TM and TE polarization, which effectively achieves the NOR and AND logic functions. In (a), EWs are incident in TE polarization with AND gates, while in (b), EWs are incident in TM polarization with NOR gates.

$Tr = 0.9785$ and an output logic of "Out = 1." In other logic cases in these conditions, Tr is less than 0.1 and the output logic is "Out = 0," which adheres to the NOR logic operation of "1 NOR 0 = 0," "0 NOR 1 = 0," and "1 NOR 1 = 0." When an electromagnetic wave is incident with TE polarization, as illustrated in Fig. 2(b), only when the ABIE is adjusted to 30° and the temperature is controlled at 345 K, that is "$In_1 = 0$" and "$In_2 = 0$," a sharp TP is generated, resulting in an output logic "Out = 1." Its corresponding performance parameters are as follows: $Tr = 0.9493$ and the frequency point of TP is $f = 2.3061\alpha$. This logical operation follows the behavior of an AND logic gate: "1 AND 0 = 0," "0 AND 1 = 0," and "0 AND 0 = 0." In the case of both NOR and AND logic gates, it is evident that their output logic aligns seamlessly with the TP spectra. Simultaneously, significant differences exist in the FPs under different logic gates, indicating the potential for MLPS to implement diverse logic operations across distinct frequency ranges at varying thresholds.

To clarify that we can achieve the equivalent effect of a 280 mm liquid crystal layer through a multilayer stacking approach. We can divide the liquid crystal into 28 layers and insert a 0.02 mm SiO_2 sheet between each layer. To support this, we have conducted simulations comparing the performance of the original model with this proposed multilayered structure. The results of this comparison are presented in Sec. III of the supplementary material. If the values of B_1 and B_2 are changed, the details information can be seen in Sec. V of supplementary material.

Due to the diverse composition of the MLPS, it exhibits a degree of complexity, and as a result, there may be multiple underlying factors contributing to the presence of TP. To investigate the role of the defect layer as a potential cause of TP, we created two separate control groups in both NOR and AND logic gates. In the AND logic gate, we chose $T_0 = 345$ K and $\varphi = 30°$ to investigate the case. In Figs. 3(a) and 4, without the defect layer, a PBG is evident in the Tr and Re spectra within 2.300α–2.312α. However, with the introduction of the defect layer, the PBG is disrupted, giving rise to a distinct sharp TP with Tr up to 0.9493 at 2.3061α. In NOR logic gates, we used $T_0 = 293.15$ K and $\varphi = 0°$ to investigate the TP's underlying cause. In the absence of the defect layer, illustrated in Figs. 3(c) and 4, the Tr and Re spectra display a PBG within 1.730α–1.738α. Upon introducing the defect layer, seen in Figs. 3(d) and 4, the initial PBG undergoes modification, resulting in the emergence of a passband with T up to 0.9785 at 1.7345α. To investigate the formation of TP, Fig. 5 illustrates the distribution of electric field energy for NOR and AND logic functions depicted in Figs. 3 and 4. In AND logic gates, when EWs propagate in TE polarization through the MLPS at 2.3061α, there is a noticeable

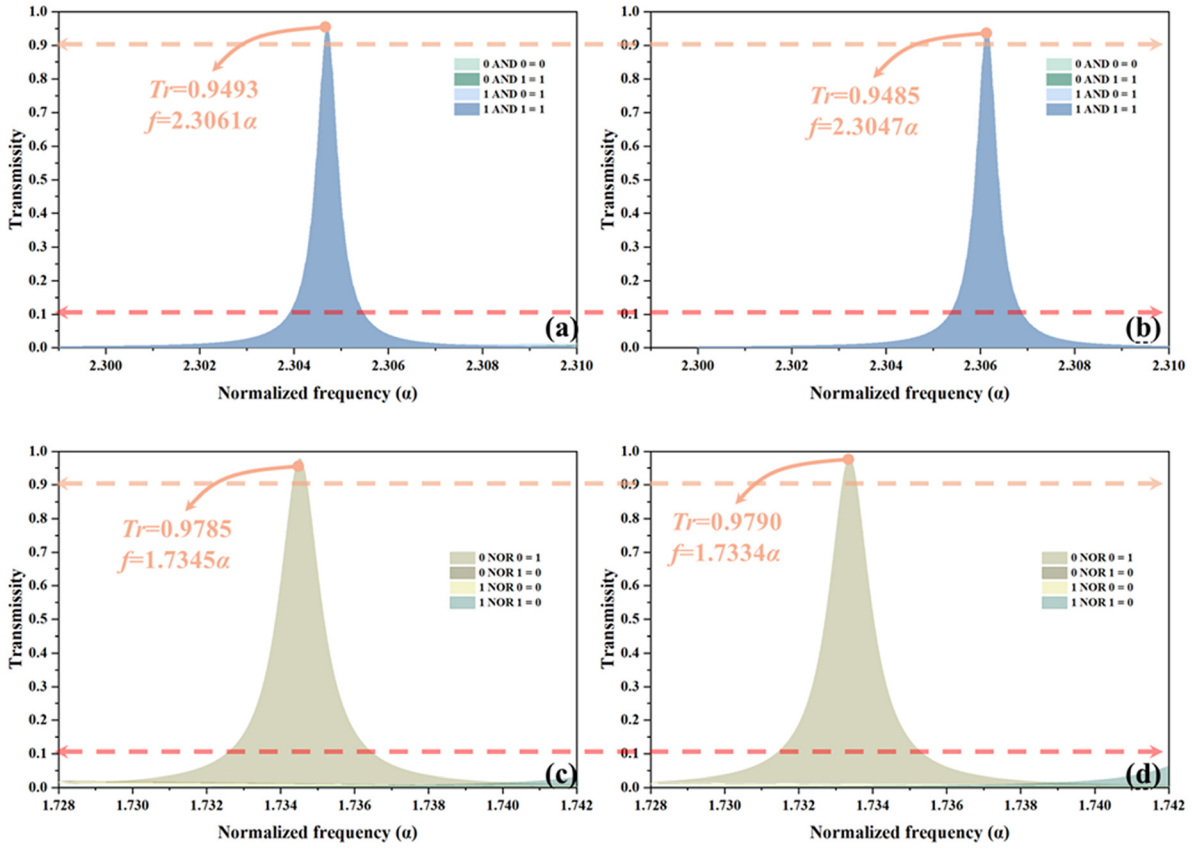

FIG. 3. (a) and (c) Transmittance spectra under TM and TE polarization, which are obtained through the simulation of a single—piece liquid—crystal. (b) and (d) Transmittance spectra under TM and TE polarization, derived from the simulation of 28 liquid—crystal pieces with a width of 10 mm, stacked with SiO_2 thin films of 0.02 mm width as spacers. It is noted that both simulation methods conform to NOR and AND logic gates, respectively.

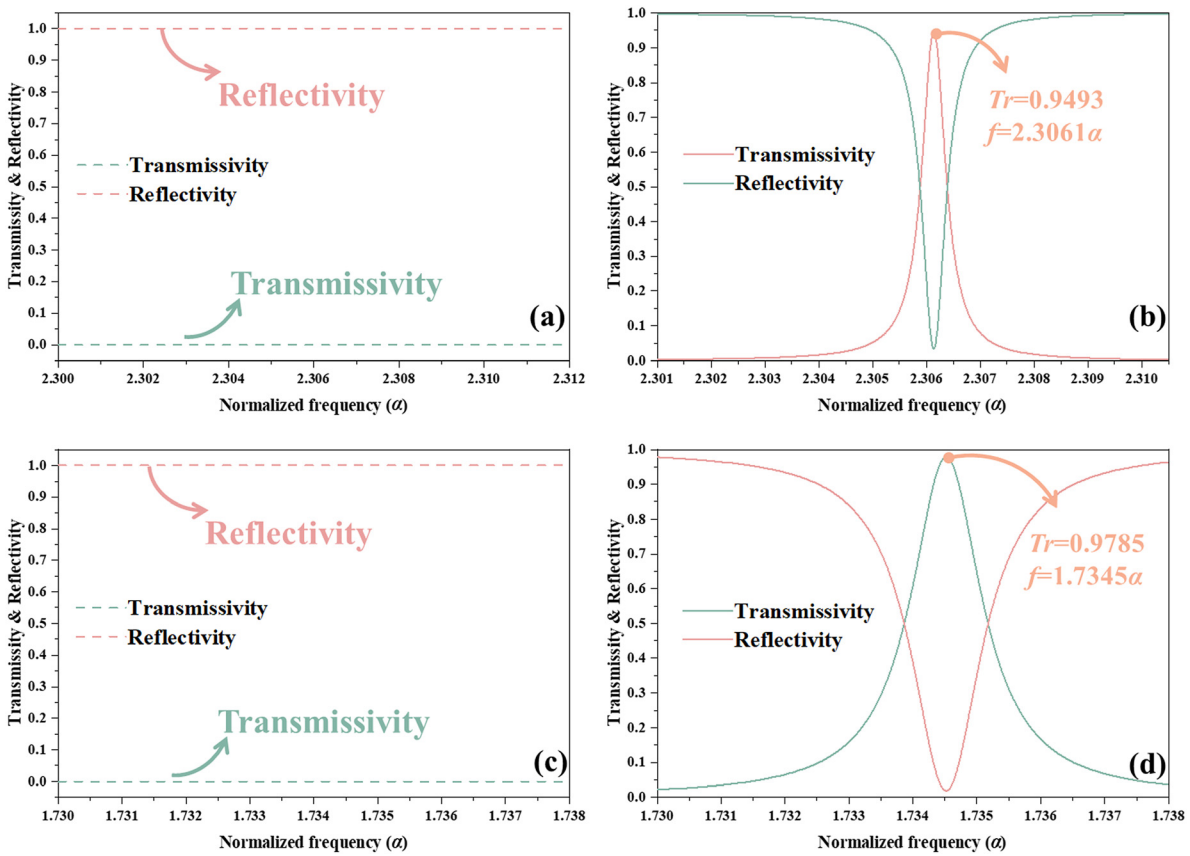

FIG. 4. Impact of the defect layer on the transmission spectra of two logic gates. (a) *Re* and *Tr* spectrum before defect layer introduction with EWs incident in TE polarization. (b) *Re* and *Tr* spectra following the introduction of the defect layer with EWs incident in TE polarization. (c) *Re* and *Tr* spectra before defect layer introduction with EWs incident in TM polarization. (d) *Re* and *Tr* spectra following the introduction of the defect layer with EWs incident in TM polarization.

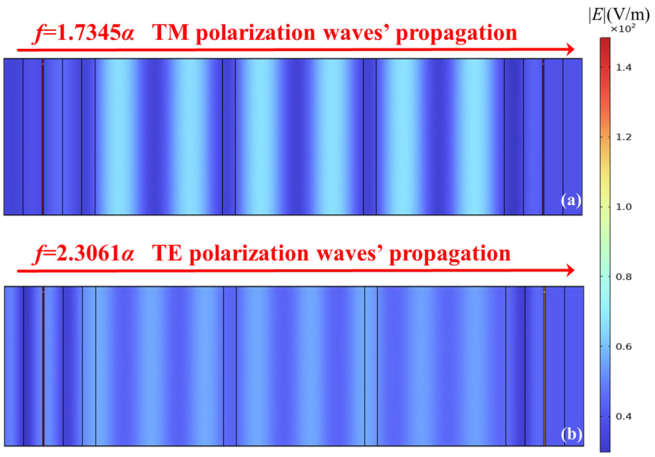

FIG. 5. The simulation diagram illustrating the distribution of electric field energy during the propagation of EWs (a) in TM polarization at $f = 1.7345\alpha$ and (b) in TE polarization at $f = 2.3061\alpha$.

concentration and enhancement of electric field energy on the surface of the plasma layer. This phenomenon induces high-frequency electron vibrations and stimulates the generation of LDMR, thereby facilitating the generation of TP. In NOR logic gates, when EWs intersect in TM polarization with the MLPS at 1.7345α, TP is generated for the same reasons as in AND logic gates. The simulation results are obtained using the 3D EM simulation software HFSS, based on the finite element method (FEM). The Floquet port positioned above the unit cell emits LP waves with $+y$ polarization vertically along the $-z$ direction.

Considering that the thickness of the dielectric layer may be affected by the process level and environmental factors during the actual processing, resulting in a certain error, Fig. 6 demonstrates the change of TP and FP in the *Tr* spectra with the unit thickness d_0 when the electromagnetic wave is incident with TM and TE polarization. With the gradual increase in the unit thickness, the TP in the *Tr* spectrum decreases gradually, and when d_0 increased to 160 mm, the TP decreases from 0.981 to 0.972 and the FP moves from 1.7339α to 1.7356α under the TM polarization condition, and the TP decreased from 0.958 to 0.924 and the FP moved from 2.3055α to 2.3073α in the

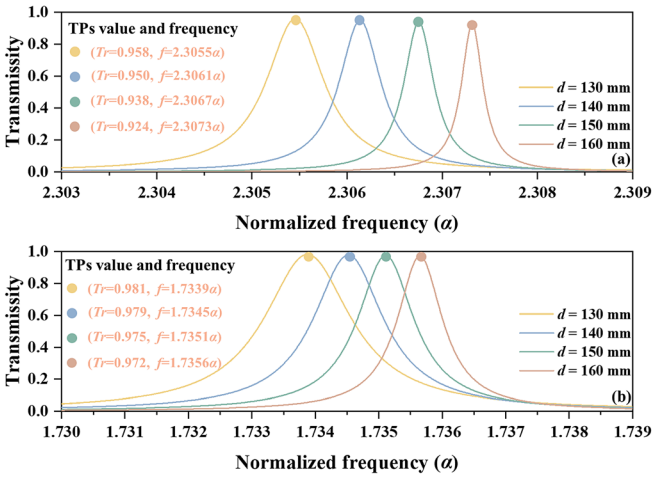

FIG. 6. The transmission spectra when EWs are incident in (a) TE polarization, and (b) TM polarization under different *d*.

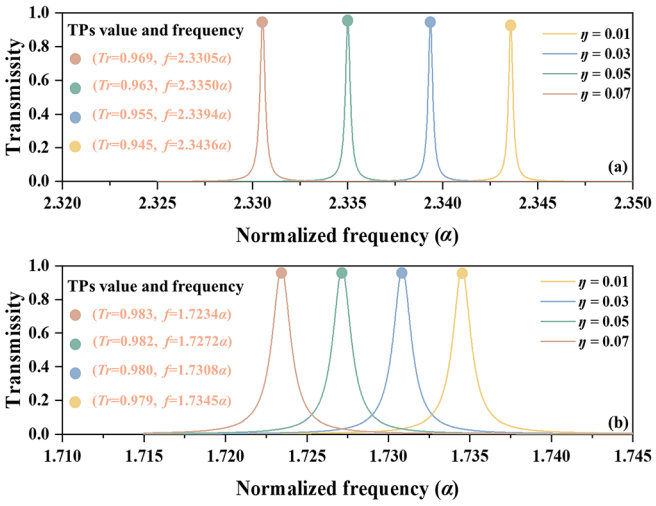

FIG. 7. The transmission spectra when EWs are incident in (a) TE polarization under and (b) TM polarization under different η.

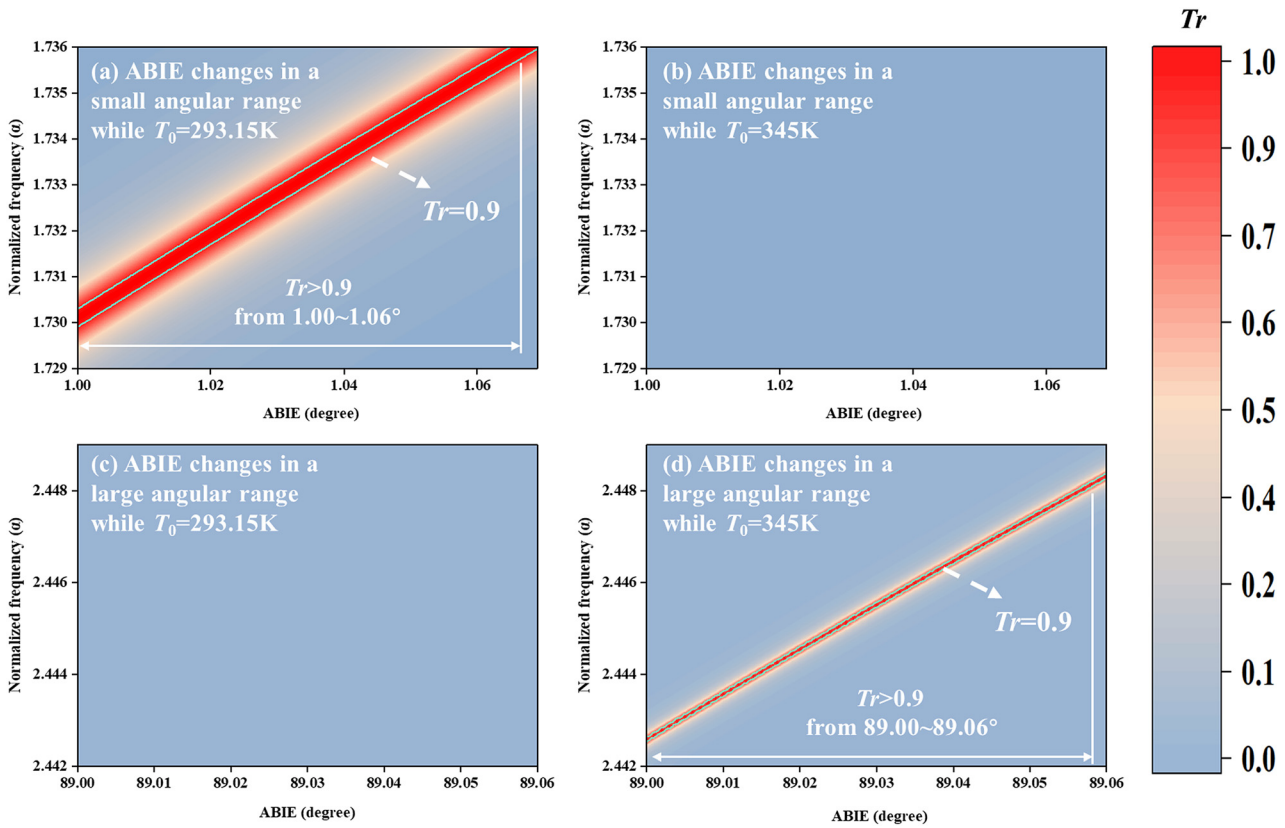

FIG. 8. The view from above TP changes with both ABIE and the normalized frequency in TM and TE polarization. In TM polarization, ABIE changes and (a) $T_0 = 293.15$ K, a sharp TP is observed within the range of 1.00°–1.06°. (b) $T_0 = 345$ K, no sharp TP can be found in the detection range. In TE polarization, ABIE changes, and (c) $T_0 = 293.15$ K, no sharp TP can be found in the range of 89.00°–89.06°. (d) $T_0 = 345$ K, there is a sharp TP in the detection range.

TE case. The findings indicate that fluctuations in unit thickness indeed affect the *Tr* spectrum to some extent. However, the peak value remains consistently above 0.9, ensuring the uninterrupted functionality of the logic gates. This suggests that both types of logic gates exhibit a degree of tolerance toward variations in unit thickness, thereby mitigating the influence of environmental factors on thickness.

As a crucial constituent of MLPS, metal–dielectric nanocomposites are influenced by the filling factor η. Figures 7(a) and 7(b) illustrate the variation of TP and FP in the Tr spectra concerning η, considering incident EWs with both TM and TE polarization. Under TM polarization, as η rises from 0.01 to 0.07, the peak elevates from 0.979 to 0.983, and the FP shifts from 1.7345α to 1.7234α. Similarly, under TE polarization, the peak decreases from 0.945 to 0.969, and the FP shifts from 2.3436α to 2.3305α. Analysis of the images reveals that both polarization modes exhibit some sensitivity in FP, with smaller peak changes observed under TM polarization and larger ones under TE polarization. Hence, in given MLPS, adjusting η can be considered to enhance performance. Furthermore, the structure's sensitivity to η suggests its capability for concurrent filling factor detection.

As one of the primary sensing methods employed by the sensor, modulation frequency facilitates the conversion of signals that are challenging to observe into photoelectric signals that are easily distinguishable. This paper presents a novel approach to sensing multiple physical quantities by establishing a linear relationship between the changes in FP and the changes in each physical quantity. Consequently, the value of each physical quantity can be indirectly determined based on FP. To provide a more visual representation of the impact of linear fitting, the coefficient of determination, denoted as R^2, has been incorporated. A value closer to 1 for R^2 indicates a stronger confirmation of the fit, signifying the enhanced explanatory power of the dependent variable concerning the independent variable.[43,44] To assess the performance of sensing, several metrics are introduced, namely *S*, *Q*, *FOM*, and *DL*. An excellent sensor is characterized by higher *S*, *Q*, and *FOM* values, as well as a lower *DL*. The relevant definitions for these metrics are provided as follows:[39]

$$S = \frac{\Delta f}{\Delta x}, \tag{19}$$

$$Q = \frac{f_T}{FWHM}, \tag{20}$$

$$FOM = \frac{S}{FWHM}, \tag{21}$$

$$DL = \frac{f_T}{20SQ}, \tag{22}$$

where Δx and Δf denote the incremental changes in physical quantities and FP, respectively. In this context, it signifies the frequency of the

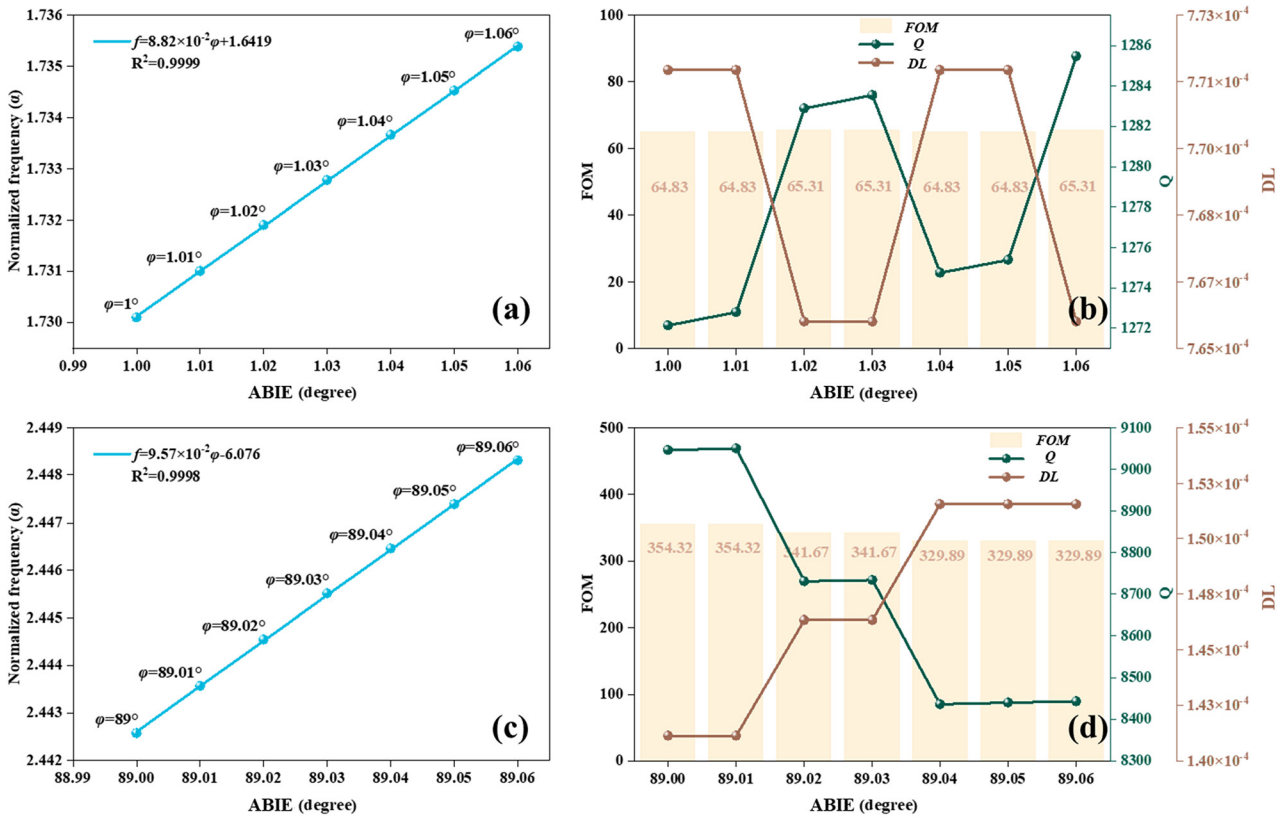

FIG. 9. The detection performance of ABIE in TM and TE polarization varies. In TM polarization, (a) the relationship between ABIE and normalized frequency is studied within a narrow angular range, and (b) the sensor's performance parameters *Q*, *FOM*, and *DL* are evaluated at various φ values. In TE polarization, (c) the correlation between ABIE and α is explored across a wide angular range, and (d) the sensor's performance parameters *Q*, *FOM*, and *DL* are assessed at different φ values.

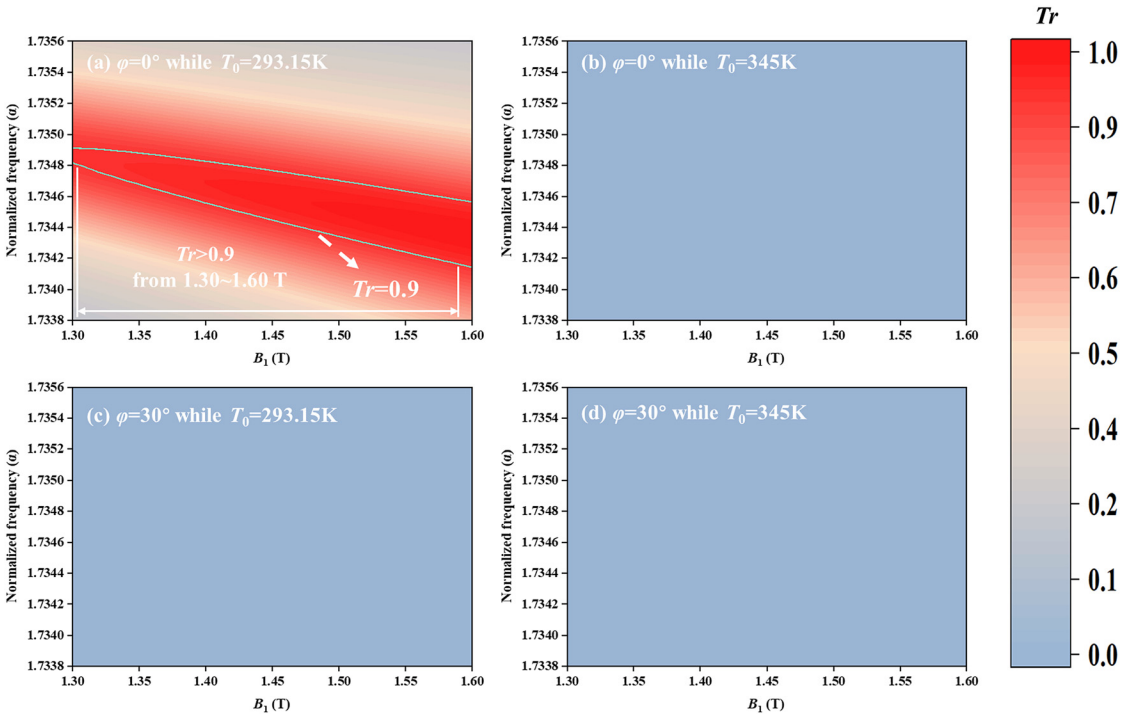

FIG. 10. The view from above TP changes with both B_1 and the α in TM polarization. When (a) $\varphi = 0^\circ$ while $T_0 = 293.15$ K, sharp TPs can be detected within the range of 1.30–1.60 T, and when (b) $\varphi = 0^\circ$ while $T_0 = 345$ K, (c) $\varphi = 30^\circ$ while $T_0 = 293.15$ K, (d) $\varphi = 30^\circ$ while $T_0 = 345$ K, no sharp TP can be found in the detection range.

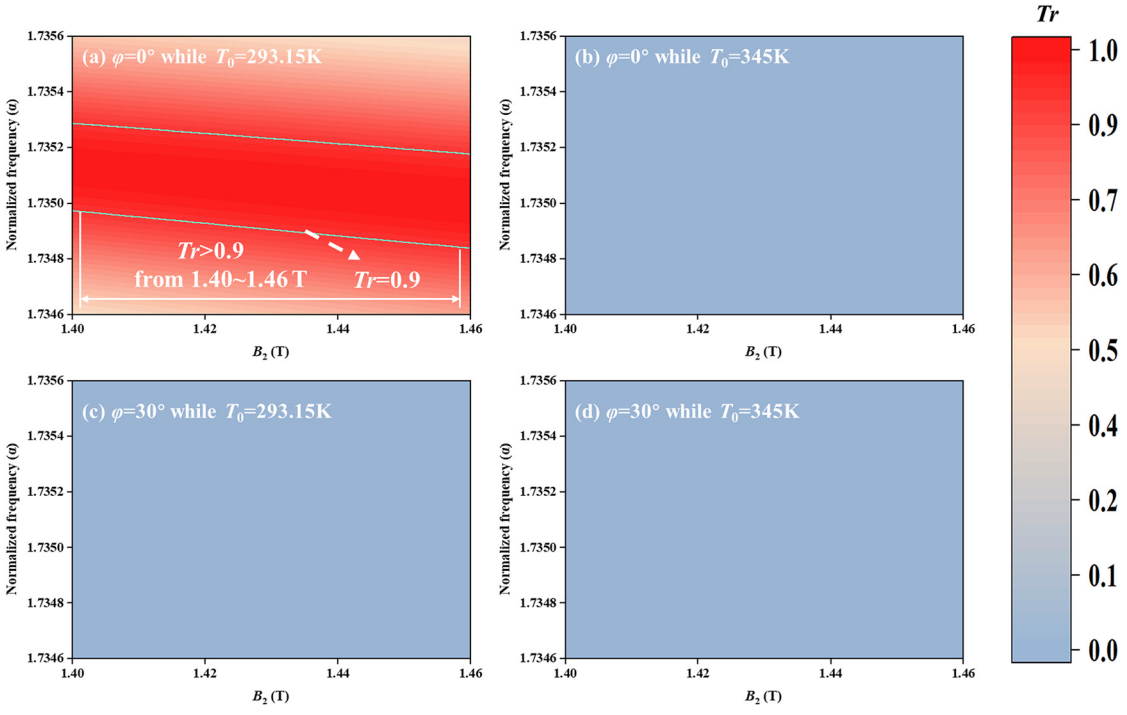

FIG. 11. The view from above TP changes with both B_2 and the α in TM polarization. When (a) $\varphi = 0^\circ$ while $T_0 = 293.15$ K, there are sharp TPs in the range of 1.40–1.46 T, and when (b) $\varphi = 0^\circ$ while $T_0 = 345$ K, (c) $\varphi = 30^\circ$ while $T_0 = 293.15$ K, (d) $\varphi = 30^\circ$ while $T_0 = 345$ K, no sharp TP can be found in the detection range.

transmission resonance peak, while FWHM stands for the half-height width.

The MLPS proves effective in detecting small-angle ABIE when incident EWs with TM polarization. Observation reveals that at a controlled temperature of $T_0 = 293.15$ K, as depicted in Fig. 8(a), resonance FP experiences a red shift with increasing ABIE within the range of 1°–1.06°, while *Tr* remains consistently above 0.9, denoted as "Out = 1." Under these conditions, with corresponding logic inputs set to "$In_1 = 0$, $In_2 = 0$," the NOR logic operation "0 NOR 0 = 1" is met. Conversely, when the temperature is controlled at $T_0 = 345$ K, as illustrated in Fig. 8(b), *Tr* falls below 0.1 within the detection range. Correspondingly, NOR logic operations are described as "0 NOR 1 = 0." This indicates the MLPS's capability to detect φ changes within the ABIE detection range while satisfying NOR logic operation criteria.

In Fig. 9(a), when the angular interval is set to 0.01°, the specific movement of the FP with the LFR of the ABIE change can be obtained, and the corresponding relation equation is obtained by linear fitting as follows: $f = (8.81 \times 10^{-2}\varphi + 1.6419)\alpha$, and $R^2 = 0.9999$, $S = 0.0882\ \alpha/\varphi$, which also demonstrates the excellent linear fitting effect and the reliability of the sensor. The values of *Q*, *FOM*, and *DL* corresponding to each ABIE detection point are shown in Fig. 9(b), which are 1.272×10^3–1.285×10^3, 64.83–$65.31\varphi^{-1}$, and 7.66×10^{-5}–$7.71 \times 10^{-5}\varphi^{-1}$, respectively, demonstrating excellent sensing performance.

The MLPS is applicable for detecting large-angle ABIE when EWs are incident in TE polarization. Similarly, at a controlled temperature $T_0 = 345$ K and varying ABIE within the range of 89°–89.06°, the FP of resonance peaks undergoes a red shift with increasing ABIE, as depicted in Fig. 8(d), while *Tr* remains consistently above 0.9, denoted as "Out = 1." Under these conditions, with corresponding logic inputs set to "$In_1 = 1$, $In_2 = 1$," the AND logic operation "1 AND 1 = 1" is satisfied. Conversely, when the temperature is controlled at $T_0 = 293.15$ K, as shown in Fig. 8(c), *Tr* falls below 0.1 within the detection range. Correspondingly, AND logic operations are described as "1 AND 0 = 0." This implies that the MLPS can detect φ changes within the ABIE detection range while simultaneously satisfying the AND logical operation. Likewise, in Fig. 9(c), the corresponding relationship equation obtained through linear fitting is represented as "$f = (9.57 \times 10^{-2}\varphi\text{-}6.076)\ \alpha$," with the corresponding R^2 and *S* values being 0.9998 and $0.0957\alpha/\varphi$. The sensing performance parameters are depicted in Fig. 9(d) as follows: $Q = 8442.45$–9046.56, $FOM = 329.89$–$354.32\varphi^{-1}$, $DL = 1.41 \times 10^{-5}$–$1.52 \times 10^{-5}\varphi^{-1}$.

Through observation, it becomes evident that the MLPS demonstrates outstanding performance in both polarization modes, aligning with the respective logic operations. Additionally, it is observed that the TM polarization condition is more adept at sensing smaller ABIEs, whereas the TE polarization condition excels in detecting larger

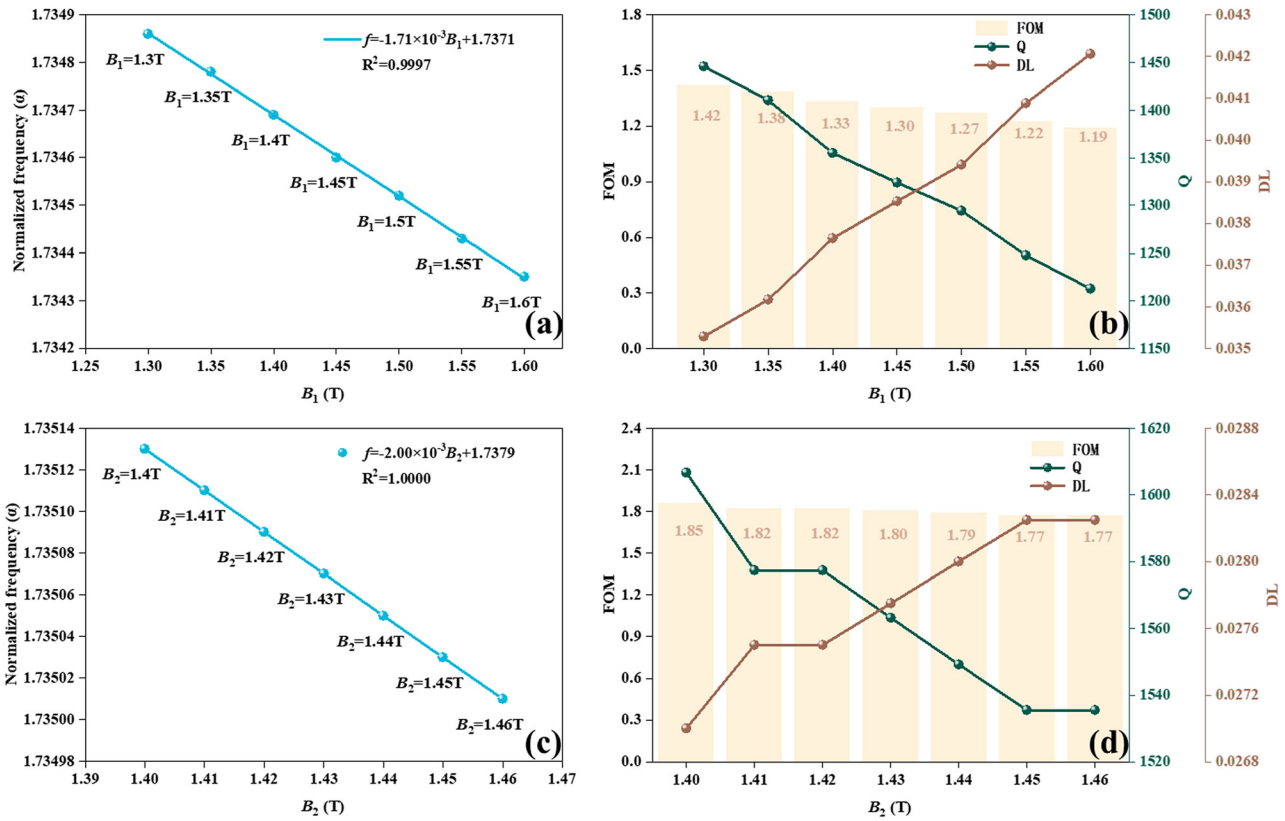

FIG. 12. In TM polarization, the detection performance of magnetic field strength is evaluated. (a) The relationship between B_1 and α is studied within the range of 1.30–1.60 T, and (b) the performance parameters of the sensor at different B_1. (c) The relationship between B_2 and α in the range of 1.40–1.46 T and (d) the performance parameters of the sensor at different B_2.

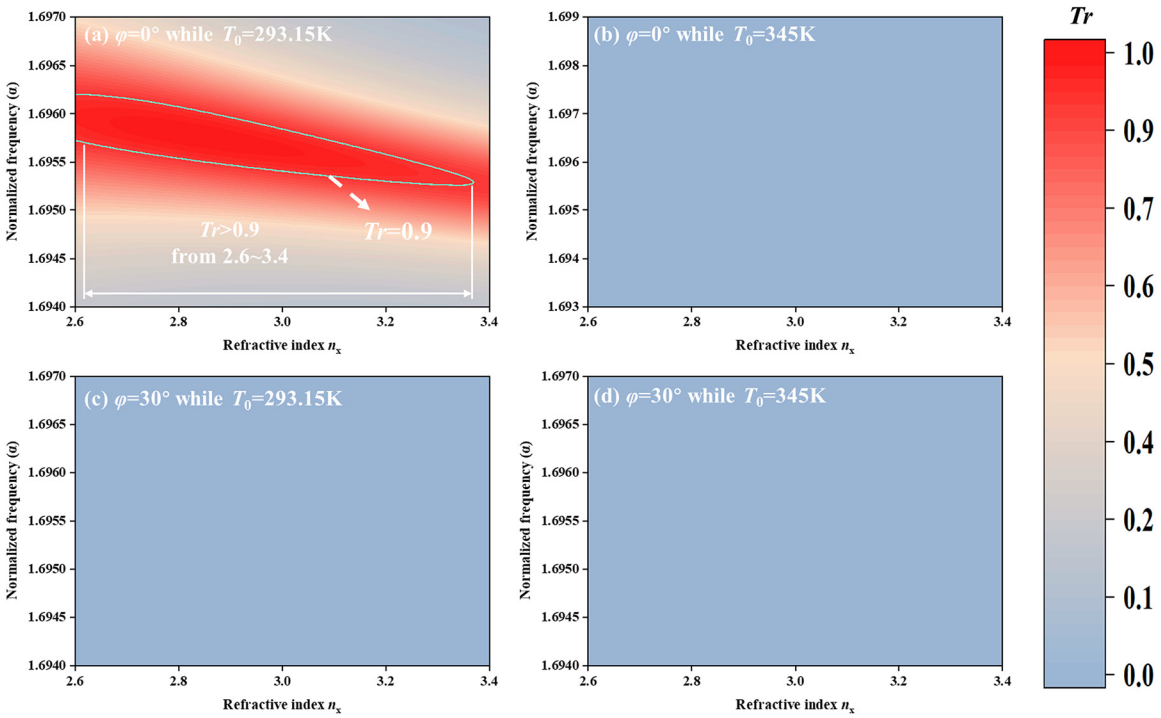

FIG. 13. The view from above TP changes with both n_x and the α in TM polarization. When (a) $\varphi = 0°$ while $T_0 = 293.15$ K, there are sharp TPs in the range of 2.60–3.30 T, and when (b) $\varphi = 0°$ while $T_0 = 345$ K, (c) $\varphi = 30°$ while $T_0 = 293.15$ K, (d) $\varphi = 30°$ while $T_0 = 345$ K, no sharp TP can be found in the detection range.

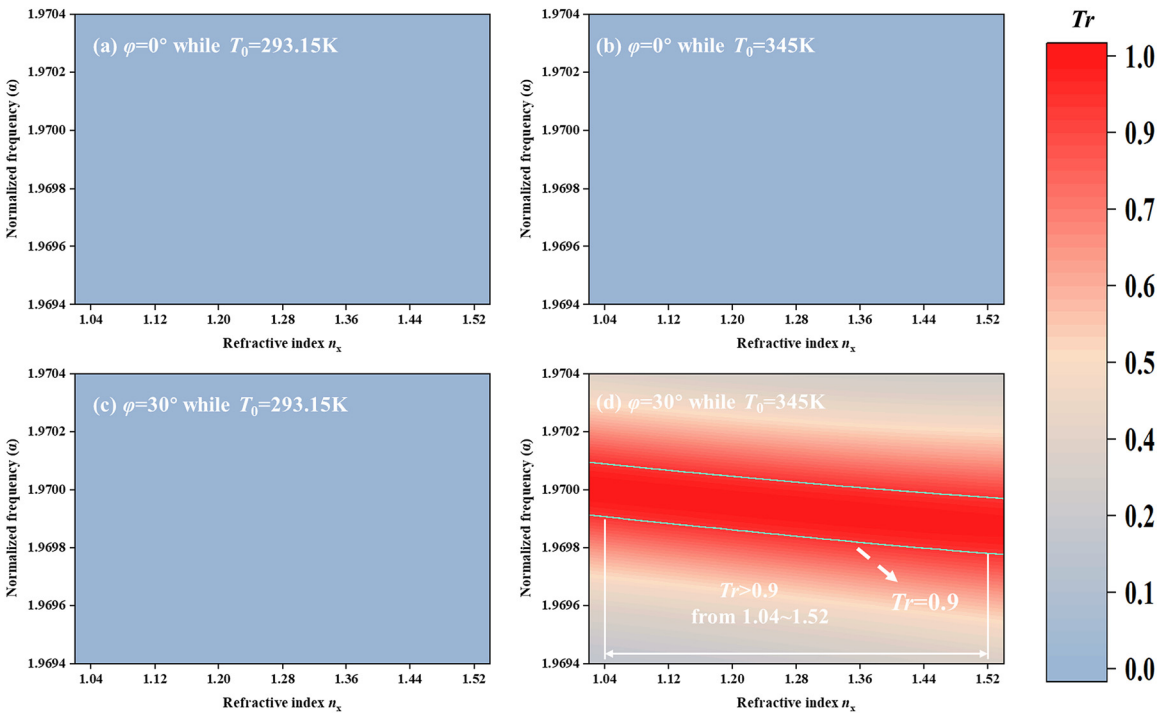

FIG. 14. The view from above TP changes with both n_x and the α in TE polarization. When (a) $\varphi = 0°$ while $T_0 = 293.15$ K, (b) $\varphi = 0°$ while $T_0 = 345$ K, and (c) $\varphi = 30°$ while $T_0 = 293.15$ K, no sharp TP can be found in the range of 1.02–1.5, and when (d) $\varphi = 30°$ while $T_0 = 345$ K, sharp TPs can be detected within the detection range.

ABIEs. This versatility provides the MLPS with a broader range of applications, enhancing the sensor's flexibility and convenience for various scenarios. Such as the demand for precise small-angle measurements in interferometers,[45] and astronomical telescopes,[46] among others, and the necessity for extensive angle measurements in radar technology,[47] satellite navigation,[48] and related domains, the MLPS in this paper offers a possible solution.

The MLPS can serve to detect magnetic field strength variations as well. Figures 10(a) and 11(a) depict the variation of FP with B_1 and B_2 when EWs are positively incident under TM polarization. At a controlled temperature of $T_0 = 293.15$ K and $\varphi = 0°$ ($In_1 = 0$, $In_2 = 0$), it is observed that B_1 within the range of 1.3 T–1.6 T yields TPs greater than 0.9 (output as "Out = 1"), similarly, B_2 in the range of 1.4–1.46 T produces TPs greater than 0.9 (also outputting "Out = 1"), and both conform to the NOR logic operation "0 NOR 0 = 1." With increasing B_1 and B_2, a red shift of the FP is induced due to alteration in the refractive indices of $plasma_1$ and $plasma_2$ caused by the additional magnetic field, consequently shifting the FP of the TP accordingly. Conversely, when the control temperature is $T_0 = 345$ K or $\varphi = 30°$, Tr drops below 0.1 within the detection range of both B_1 and B_2, leading to the disappearance of TP. Consequently, the corresponding NOR logic operations are described as "1 NOR 0 = 0," "0 NOR 1 = 0," and "1 NOR 1 = 0." This signifies that within the detection range of B_1 and B_2, MLPS can detect changes in magnetic field strength while simultaneously satisfying NOR logic operations.

The linear fitting of the LFR of B_1 with FP is illustrated in Fig. 12(a), yielding the relation $f = (-1.71 \times 10^{-3} B_1 + 1.7371)\alpha$, with a calculated R^2 value of 0.9997 and $S = 0.0017$ α/T. This demonstrates excellent linear fitting performance. The correlation performance parameters are displayed in Fig. 12(b), indicating $Q = 1212.832$–1445.717, $FOM = 1.189$–1.417 T^{-1}, $DL = 3.53 \times 10^{-2}$–4.21×10^{-2} T^{-1}. Similarly, the LFR of B_2 with FP can be obtained from Fig. 12(c), resulting in $f = (2.0 \times 10^{-3} B_2 + 1.7379)\alpha$, with an R^2 value of 1 and $S = 0.002\alpha$/T. This also showcases outstanding sensor performance. The relevant performance parameters are presented in Fig. 12(d) for Q, FOM, and DL ranges are 1535.407–1606.602, 1.77–1.85T^{-1}, and 2.70–2.82T^{-1}, respectively.

Under TM polarization, the detection of magnetic field strength demonstrates excellent performance for both B_1 and B_2, while following the NOR logic operation. In practical applications, the broader sensing range of B_1 can be utilized for initial rough detection, followed by the employment of B_2 for finer sensing. Additionally, by comparing the sensing results of B_1 and B_2, inspection and correction can be achieved for the sensing outcomes. This multi-scale magnetic field

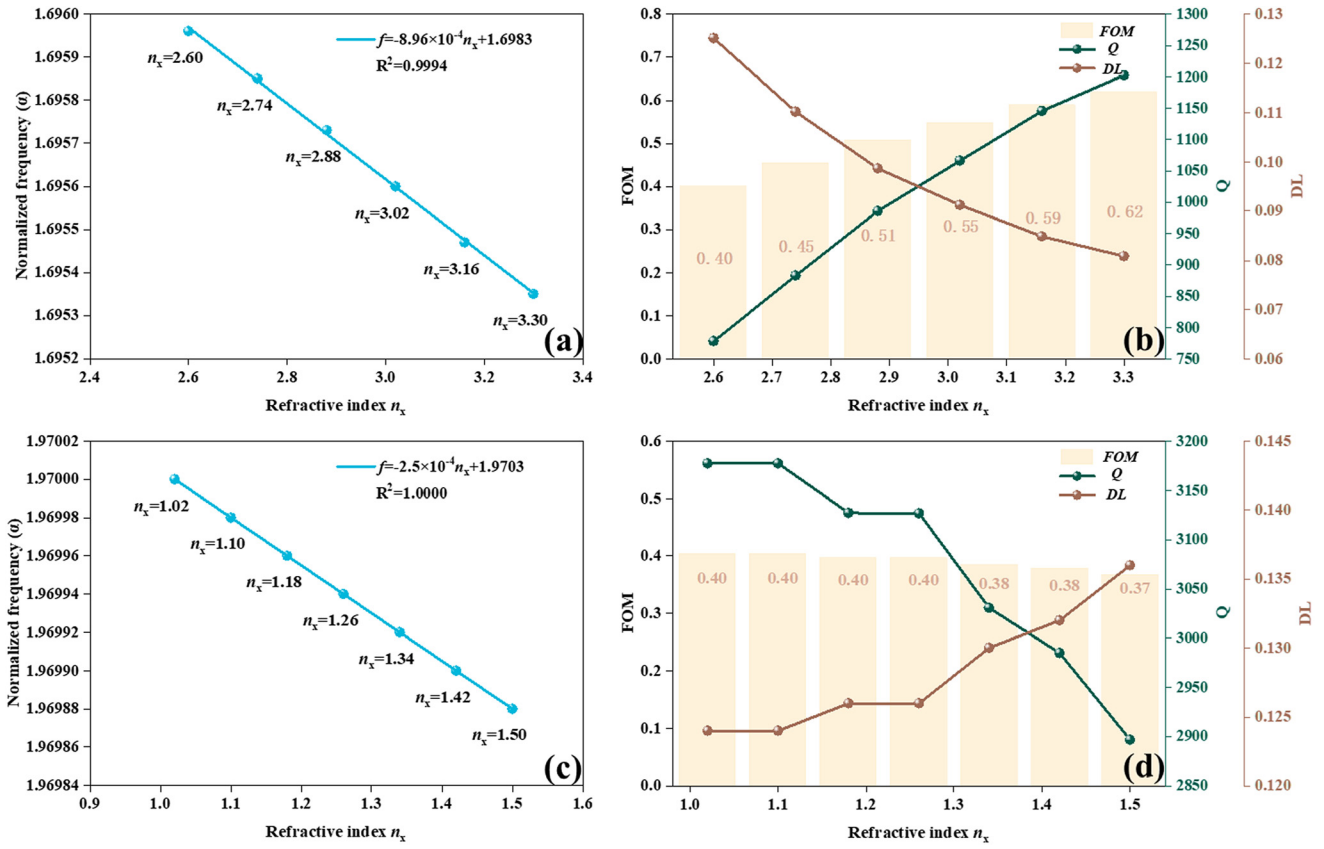

FIG. 15. The performance of RI is examined in both TM and TE polarization modes. In TM polarization, (a) the relationship between n_x and α in the range of 2.6–3.3, and (b) the performance parameters of the sensor at different n_x. In TE polarization, (c) the relationship between n_x and α in the range of 1.02–1.5 and (d) the performance parameters of the sensor at different n_x.

sensing characteristic endows the MLPS with robustness against magnetic field data interference, enabling it to better adapt to the complexity of magnetic field signals and achieve more precise prediction and analysis of sensing results.

The need for RI detection is critical across diverse fields, including biology,[49] chemistry,[50] physics,[51] and others. Consequently, there is significant interest in sensors designed for RI detection. The sensing performance of MLPS discussed in this paper also possesses the capacity to accurately detect RI. To investigate the capability of MLPS in RI detection, this paper employs a layered object with a consistent thickness ($d_n = 0.1d_0$) and varying n_x within a specified range. This object is positioned on the incident plane of EWs, and an RI sensor is developed by establishing a linear relationship between the FP and the n_x of the object. As depicted in Figs. 13(a) and 14(d), when EWs are incident in TM and TE polarization modes, respectively, the resulting TPs remain greater than 0.9 within the RI ranges of 2.6–3.3 and 1.02–1.5, respectively. This indicates outputs of "Out = 1," corresponding to the logical operation modes of "0 NOR 0 = 1," and "1 AND 1 = 1" logic operations, respectively. However, as illustrated in Figs. 13(b)–13(d) and 14(a)–14(c), in the other three logic operation conditions, TP vanishes, and the corresponding NOR logic operations are described as "1 NOR 0 = 0," "0 NOR 1 = 0," and "1 NOR 1 = 0." Similarly, *Tr* is consistently less than 0.1, aligning with "1 AND 0 = 0," "0 AND 1 = 0," and "0 AND 0 = 0" logical operations. This signifies that the MLPS can simultaneously follow the corresponding logical operation rules and achieve RI sensing within the detection range under both polarization modes.

When EWs are incident in TM polarization, n_x ranges from 2.6 to 3.3 with an increment of 0.14 at $T_0 = 293.15$ K and $\varphi = 0°$, as depicted in Fig. 15(a). The corresponding LFR is represented as $f = (-8.96 \times 10^{-4}\boldsymbol{n_x} + 1.6983)\alpha$. Additionally, the values of S and R^2 are 8.96×10^{-4} α/RIU and 0.9994, respectively. Similarly, when EWs are incident in TE polarization, as illustrated in Fig. 15(c), the corresponding LFR is $f = (-2.5 \times 10^{-4}\boldsymbol{n_x} + 1.9703)\alpha$, with n_x ranging from 1.02 to 1.5 with an interval of 0.08 under the conditions of $T_0 = 345$ K and $\varphi = 30°$. The values of S and R^2 are 2.5×10^{-4} α/RIU and 1, respectively, demonstrating a robust correlation between FP and n_x. The values of *Q*, *FOM*, and *DL* for both polarization modes are displayed in Figs. 15(b) and 15(d). When TM polarization is utilized, the range of *Q* is 777.963–1202.376, *FOM* is 0.400–0.618 RIU^{-1}, and *DL* is 0.08–0.12 RIU^{-1}. On the other hand, when TE polarization is employed, the range of *Q* is 2896.882–3177.419, *FOM* is 0.368–0.403 RIU^{-1}, and *DL* is 0.124–0.136 RIU^{-1}. These results collectively indicate excellent performance in RI detection for both polarization. Additionally, considering the different RI measurement ranges for the two polarization modes, the MLPS can be tailored to accommodate various sensing requirements.

Temperature detection holds significant importance in electromagnetic compatibility testing,[52] enabling the monitoring of equipment temperature variations under different operating conditions to assess its immunity to electromagnetic interference and radiation. Consequently, temperature sensing in this research is of paramount significance. The MLPS introduced in this paper also encompasses

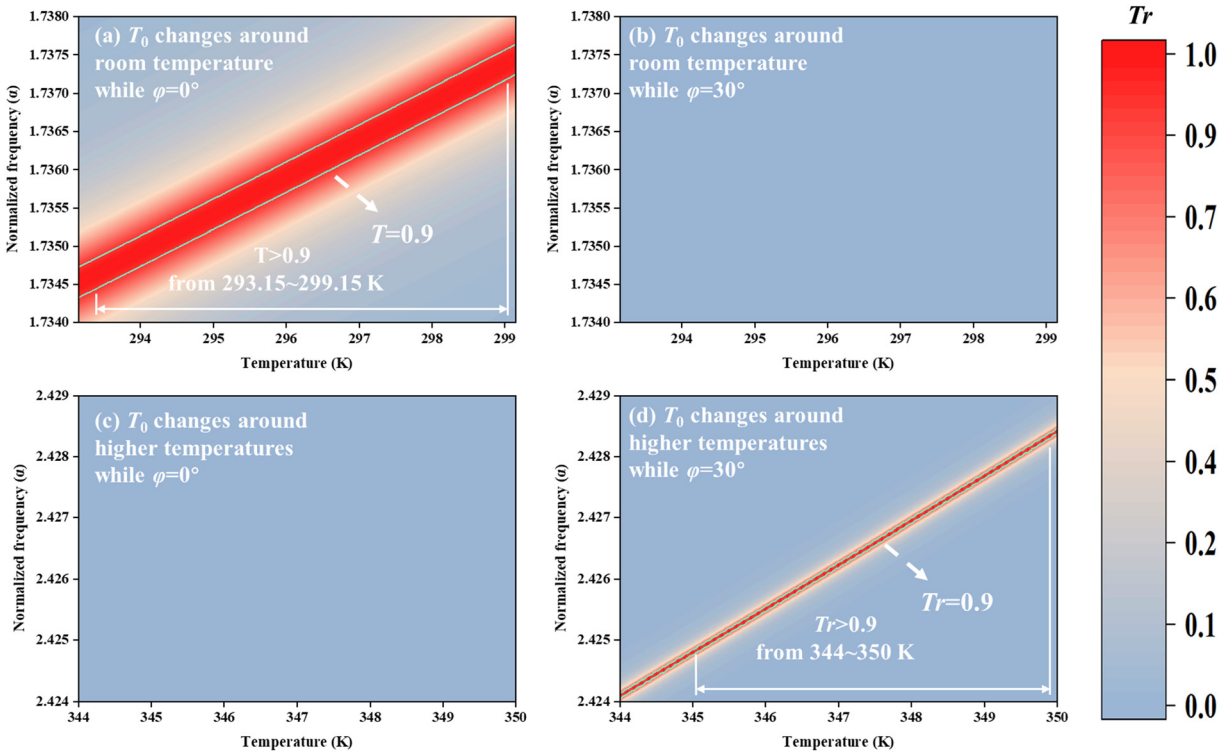

FIG. 16. The perspective of TP changes with temperature and the α in both TM and TE polarization. In TM polarization, T_0 changes, and (a) $\varphi = 0°$, there is a sharp TP in the range of 293.15–299.15 K. (b) $\varphi = 30°$, no sharp TP can be found in the detection range. In TE polarization, T_0 changes, and (c) $\varphi = 0°$, no sharp TP can be found in the range of 344–350 K. (d) $\varphi = 30°$, there is a sharp TP in the detection range.

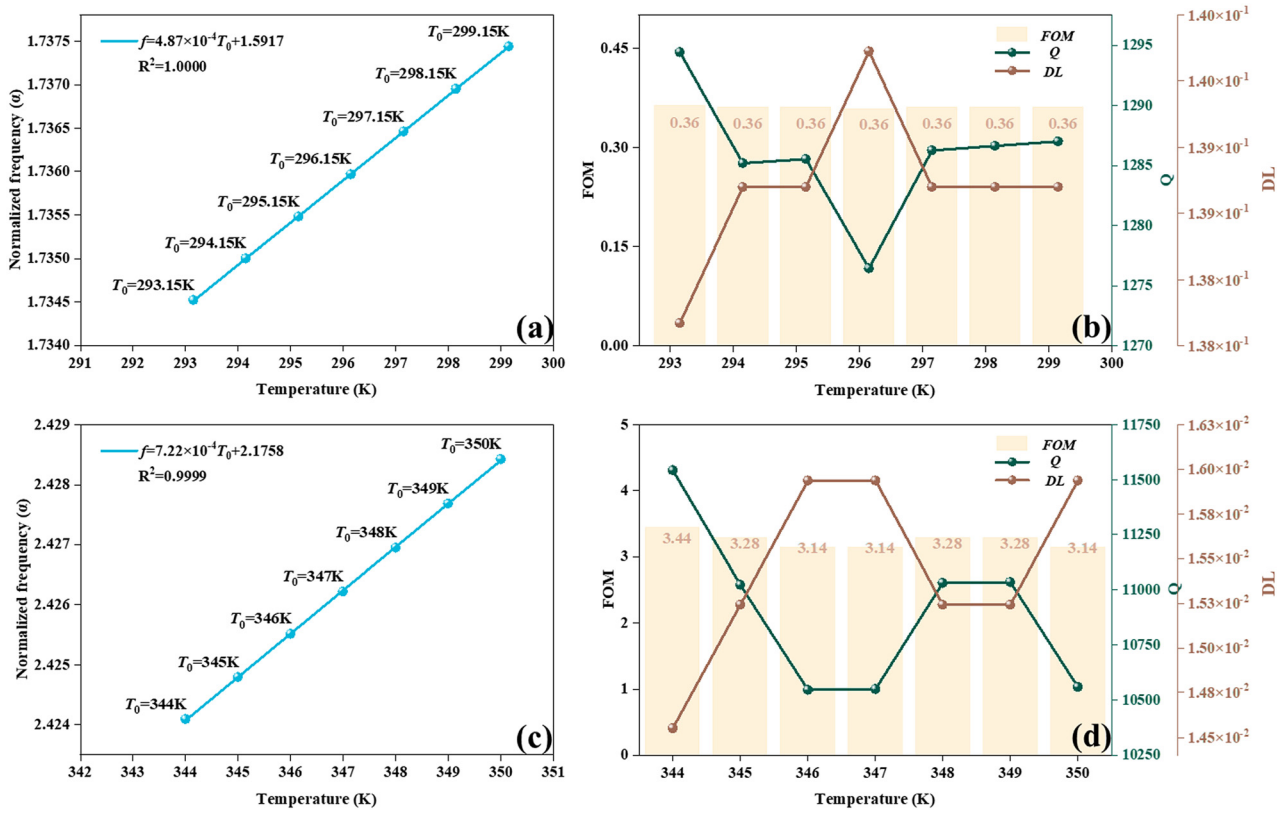

FIG. 17. The detection performance of temperature varies in TM and TE polarization. In TM polarization, (a) the LFR across T_0 and α near room temperature, along with (b) the sensor's performance metrics at various T_0 values. For TE polarization, (c) the LFR spanning T_0 and α at elevated temperatures, along with (d) the sensor's performance metrics across different T_0 values.

temperature-sensing functionality. Under TM polarization, the MLPS can be utilized for temperature sensing near room temperature ($T_0 = 293.15$ K). As depicted in Fig. 16(a), under $\varphi = 0°$, when temperature varies within the range of 293.15–299.15 K, all TPs exhibit values greater than 0.9, indicating "Out = 1." Conversely, when $\varphi = 30°$, TPs are consistently less than 0.1, signifying that temperature sensing also adheres to the principles of "0 NOR 0 = 1" and "1 NOR 0 = 0" NOR logic operations. The MLPS can also be utilized for higher temperature sensing under TE polarization conditions. As illustrated in Fig. 16(d), under $\varphi = 30°$, when T_0 varies within the range of 344–350 K, TPs remain greater than 0.9, indicating "Out = 1." Conversely, when $\varphi = 0°$, TPs are less than 0.1, indicating that temperature sensing follows "1 AND 1 = 1," and "1 NOR 0 = 0" AND logic operations.

Figures 17(a) and 17(c) show the LFR for temperature sensing that satisfies "0 NOR 0 = 1," and "1 AND 1 = 1" for TM and TE polarization, $f = (4.87 \times 10^{-4}\, T_0 + 1.5917)\alpha$ and $f = (7.22 \times 10^{-4}\, T_0 + 2.1758)\alpha$, respectively. The corresponding S is 4.87×10^{-4} and 7.22×10^{-4} α/K, respectively. The values of R^2 are 1 and 0.9999, indicating the high reliability of the LFR. Detailed values of Q, *FOM*, and *DL* for the corresponding ranges under TM and TE polarization are presented in Figs. 17(b) and 17(d), respectively:1276.449–1294.418, and 1.056×10^3–1.154×10^3, 0.360–0.363 K^{-1}, and 3.138–3.437 K^{-1}, 0.138–0.139 K^{-1}, and 0.0146–0.0160 K^{-1}, which indicates that MLPS-based temperature sensing exhibits excellent performance across two different ranges. Additionally, it enables temperature sensing within various ranges according to the temperature requirements of different scenarios.

In order to further study the mutual influence among the sensitivities of these several physical quantities, we observe the changes in the sensitivities of each physical quantity by changing d_0, as shown in Fig. 18.

The provided graphs offer a detailed exploration of the relationships between the d_0 and the S of various physical quantities in both TM and TE modes. In Fig. 18(a), the S of ABIE and are depicted. In the TM mode, as d_0 increases from 0.09 to 0.21 μm, the S of ABIE increases gradually from 8.65×10^{-2} to 8.87×10^{-2} α/°. In the TE mode, the S of ABIE rises 9.23×10^{-2} to 9.73×10^{-2} α/°. In Fig. 18(b), focusing on the S of T_0 in TM and TE modes, as d_0 increases from 0.09 to 0.21, the S of T_0 in the TM mode rises from 4.78×10^{-4} to 4.9×10^{-4} α/K, and in the TE mode, it increases from 7.05×10^{-4} to 7.28×10^{-4} α/K. The higher S of in the TM mode suggests a more favorable interaction between and the TM mode with increasing. In Fig. 18(c), the S of and B_1 and B_2 is presented. In both TM and TE modes, as d_0 increases, the S of B_1 and B_2 exhibits fluctuating behavior. This indicates a complex coupling relationship between B_1, B_2, and d_0. In Fig. 18(d), the n_x under the two polarization modes seems not to be affected and remains constant.

Regarding the coupling relationships among the S of these physical quantities, the following observations are made: The increase in S

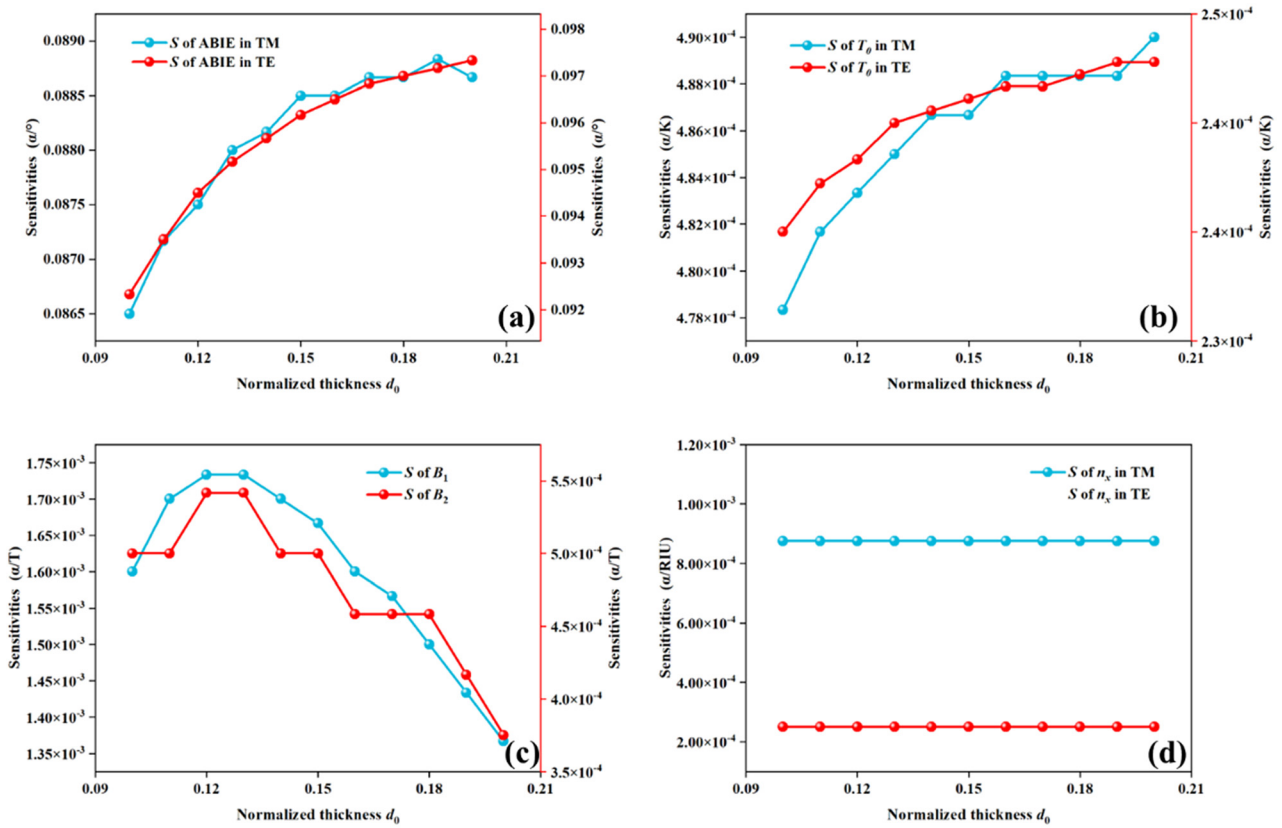

FIG. 18. The S variations of different physical quantities in TM and TE modes with respect to the normalized thickness d_0. In TM mode, (a) shows the sensitivities of ABIE and T_0 as d_0 varies, along with (b) the comparison of sensitivities of T_0 in TM and TE modes. For TE mode, (c) presents the sensitivities of B_1 and B_2 with the change of d_0, along with (d) the sensitivities of n_x in TM and TE modes as n_x changes.

TABLE II. Performance comparison of MLPS with published reports.

Reference	Multi-function	Detection of physical properties			Sensitivities	Logic gate
53	No	None			None	AND
54	No	None			None	NOR
55	No	Temperature	Range	0–40 °C	5 nm/°C	None
56	No	RI	Range	1.34–1.41	6500 nm/RIU	None
57	No	RI	Positive range	1.35–2.09	132 MHz RIU^{-1}	None
			Negative range	1–1.57	40.7 MHz RIU^{-1}	
58	Yes	RI	Range	1.455–1.469	56.815 dBm RIU^{-1}	None
		Temperature	Range	22–42 °C	56.815 dBm RIU^{-1}	
This work	Yes	RI	TM polarization	2.6–3.3	8.75×10^{-4} $(2\pi c/d)$/RIU	NOR
		Temperature		293.15–299.15 K	4.87×10^{-4} $(2\pi c/d)$/K	
		MFS		1.3–1.6 T and 1.4–1.46T	1.7×10^{-3} $(2\pi c/d)$/T and 2×10^{-3} $(2\pi c/d)$/T	
		ABIE		1°–1.06 °	0.0882 $(2\pi c/d)$/°	
		RI	TE polarization	1.02–1.05	2.5×10^{-4} $(2\pi c/d)$/RIU	AND
		Temperature		344–350 K	7.22×10^{-4} $(2\pi c/d)$/K	
		ABIE		89–89.06 °	0.0957 $(2\pi c/d)$/°	

of T_0 in both TM and TE modes seems to be accompanied by a relatively small increase in S of ABIE. This suggests that the S growth of T_0 may have a partially suppressing effect on the S growth rate of ABIE's. For B_1 and B_2, their fluctuating S implies that changes in d_0 may lead to alternating enhancement and suppression effects among the S of these two quantities. For example, an increase in d_0 may cause a decrease in the S of B_1 while simultaneously causing an increase in the S of B_2, indicating a trade-off relationship between their S at certain d_0 values. Overall, the S of these physical quantities is intricately linked, and changes in d_0 can lead to various coupling effects among them, which are essential for understanding the electromagnetic properties and interactions of these quantities.

Based on the research findings presented above, the MLPS proposed in this study exhibits exceptional performance within the realm of electromagnetic fields. This structure not only serves the purpose of detecting ABIE but also possesses the capability to measure magnetic field intensity, RI, and temperature. Furthermore, the MLPS supports multi-precision detection in both positive and negative directions, making it adaptable to specific environmental requirements. To evaluate the performance of the sensor, we have introduced several key indicators, including *S*, *Q*, *FOM*, and *DL*, all of which have demonstrated excellent results. As illustrated in Table II, MLPS is described systematically and intuitively. A comparative analysis of the MLPS presented against previously discovered devices with exceptional performance, considering factors such as versatility and physical quantity detection, leads to the conclusion that the MLPS presented here represents an advancement over prior methods and holds a superior position in the field. This paper places its primary emphasis on theoretical innovation and research method development. A thorough analysis of parameters such as dielectric thickness and RI leads to the determination of more suitable values. Details on the multi-function devices[59,60] and specific applications of the given devices can be seen in Sec. VI of the supplementary material.

IV. CONCLUSION

In conclusion, MLPS composed of plasma and liquid crystal materials with different logic gates and multiple physical quantities' detection under TM and TE polarization is theoretically studied. The incorporation of liquid crystal and plasma into the MLPS endows it with tunability, allowing it to respond to external factors such as magnetic fields and temperature. Additionally, those components serve as a defect layer capable of exciting LDMR, leading to the generation of sharp TPs. Two distinct logic gates are established on both the TM and TE polarization modes. The switching between NOR and AND logic gates is achieved through different polarization, and the logic output is determined by detecting the TP value. By establishing a linear relationship between the frequency shift of FP and various physical parameters such as RI, magnetic field B, temperature T_0, and ABIE, the MLPS can function as a versatile sensor for multiple physical quantities. Under TM and TE polarization, the detection ranges of RI, B, T_0, and ABIE are 2.6–3.3 and 1.02–1.5, 1.3–1.6 T and 1.4–1.46 T, 293.15–299.15 K and 344–350 K, and 1–1.06° and 89–89.06°, respectively. Finally, when evaluated based on parameters such as *S*, *Q*, *FOM*, and *DL*, the MLPS demonstrates outstanding sensing performance. Such an MLPS with two types of logic gates, and multi-function, can not only play a huge role in integrated circuits, integrated information processing, sensors, and other fields but also provide a solution for multi-function devices that require multiple scenarios.

SUPPLEMENTARY MATERIAL

See the supplementary material for the fabrication and experiment processes of the given MLPS.

ACKNOWLEDGMENTS

This work was supported by the National College Students Innovation and Entrepreneurship Training Program (Grant No. 202410293018Z).

AUTHOR DECLARATIONS

Conflict of Interest

The authors have no conflicts to disclose.

Author Contributions

Na Pei: Formal analysis (lead); Resources (lead); Validation (lead); Writing – original draft (lead). **Lijie Huang:** Methodology (lead); Software (lead); Validation (lead); Visualization (lead). **Hai-Feng Zhang:** Conceptualization (lead); Project administration (lead); Supervision (lead); Writing – review & editing (lead).

DATA AVAILABILITY

The data that support the findings of this study are available from the corresponding author upon reasonable request.

REFERENCES

[1]A. H. Aly, S. E.-S. A. Ghany, B. M. Kamal, and D. Vigneswaran, "Theoretical studies of hybrid multifunctional $YaBa_2Cu_3O_7$ photonic crystals within visible and infra-red regions," Ceram. Int. **46**, 365–369 (2020).
[2]T. Kim, E. S. Yu, Y. G. Bae, J. Lee, I. S. Kim, S. Chung, S. Y. Lee, and Y. S. Ryu, "Asymmetric optical camouflage: Tuneable reflective color accompanied by the optical Janus effect," Light **9**, 175 (2020).
[3]H. Wang, S. Yang, S.-N. Yin, L. Chen, and S. Chen, "Janus suprabead displays derived from the modified photonic crystals toward temperature magnetism and optics multiple responses," ACS Appl. Mater. Interfaces **7**, 8827–8833 (2015).
[4]Q. He, H. Vijayamohanan, J. Li, and T. M. Swager, "Multifunctional photonic janus particles," J. Am. Chem. Soc. **144**, 5661–5667 (2022).
[5]T. Zentgraf, J. Valentine, N. Tapia, J. Li, and X. Zhang, "An optical "Janus" device for integrated photonics," Adv. Mater. **22**, 2561–2564 (2010).
[6]J. C. Knight *et al.*, "Photonic band gap guidance in optical fibers," Science **282**, 1476–1478 (1998).
[7]H. Wang, P. Liu, Y. Ke, Y. Su, L. Zhang, N. Xu, S. Deng, and H. Chen, "Janus magneto–electric nanosphere dimers exhibiting unidirectional visible light scattering and strong electromagnetic field enhancement," ACS Nano. **9**, 436–448 (2015).
[8]S. Swarnakar, S. Kumar, and S. Sharma, "Performance analysis of all-optical full-adder based on two-dimensional photonic crystals," J. Comput. Electron. **17**, 1124–1134 (2018).
[9]L. H. Peng, J. H. Smet, T. P. E. Broekaert, and C. G. Fonstad, "Transverse electric and transverse magnetic polarization active intersubband transitions in narrow InGaAs quantum wells," Appl. Phys. Lett. **61**, 2078–2080 (1992).
[10]S. Kumar, Chanderkanta, and S. K. Raghuwanshi, "Design of optical reversible logic gates using electro-optic effect of lithium niobate based Mach–Zehnder interferometers," Appl. Opt. **55**, 5693 (2016).
[11]J. Knapczyk-Korczak, J. Zhu, D. P. Ura, P. K. Szewczyk, A. Gruszczyński, L. Benker, S. Agarwal, and U. Stachewicz, "Enhanced water harvesting system and mechanical performance from Janus fibers with polystyrene and cellulose acetate," ACS Sustainable Chem. Eng. **9**, 180–188 (2021).

[12]J. Jia, Y. Peng, X.-J. Zha, K. Ke, R.-Y. Bao, Z.-Y. Liu, M.-B. Yang, and W. Yang, "Janus and heteromodulus elastomeric fiber mats feature regulable stress redistribution for boosted strain sensing performance," ACS Nano. **16**, 16806–16815 (2022).
[13]L. Miao, G. Liu, and J. Wang, "Ag-nanoparticle-bearing poly(vinylidene fluoride) nanofiber mats as Janus filters for catalysis and separation," ACS Appl. Mater. Interfaces **11**, 7397–7404 (2019).
[14]M. F. Picardi, C. P. T. McPolin, J. J. Kingsley-Smith, X. Zhang, S. Xiao, F. J. Rodríguez-Fortuño, and A. V. Zayats, "Integrated Janus dipole source for selective coupling to silicon waveguide networks," Appl. Phys. Rev. **9**, 021410 (2022).
[15]M. J. Bauer, X. Wen, P. Tiwari, D. P. Arnold, and J. S. Andrew, "Magnetic field sensors using arrays of electrospun magnetoelectric Janus nanowires," Microsyst. Nanoeng. **4**, 37 (2018).
[16]K. Vijaya Shanthi and S. Robinson, "Two-dimensional photonic crystal based sensor for pressure sensing," Photonic Sens. **4**, 248–253 (2014).
[17]M. Pirzadi, A. Mir, and D. Bodaghi, "Realization of ultra-accurate and compact all-optical photonic crystal OR logic gate," IEEE Photonics Technol. Lett. **28**, 2387–2390 (2016).
[18]E. Veisi, M. Seifouri, and S. Olyaee, "A novel design of all-optical high speed and ultra-compact photonic crystal AND logic gate based on the Kerr effect," Appl. Phys. B **127**, 70 (2021).
[19]A. Mohebzadeh-Bahabady and S. Olyaee, "All-optical NOT and XOR logic gates using photonic crystal nano-resonator and based on an interference effect," IET Optoelectron. **12**, 191–195 (2018).
[20]S. Poonguzhali, A. Sivasangari, P. Ajitha, I. Rajkumar, A. Sridevi, and S. K. Danasegaran, "Design and performance analysis of smart photonic sensors for industrial applications," Curr. Appl. Phys. **39**, 183–189 (2022).
[21]Y. H. Chen, W. H. Shi, L. Feng, X. Y. Xu, and M. Y. Shang-Guan, "Study on simultaneous sensing of gas concentration and temperature in a one-dimensional photonic crystal," Superlattices Microstruct. **131**, 53–58 (2019).
[22]B. Maeng, H. Chang, and J. Park, "Photonic crystal-based smart contact lens for continuous intraocular pressure monitoring," Lab Chip **20**, 1740–1750 (2020).
[23]X.-X. Wang, Z. Guo, J. Song, H. Jiang, H. Chen, and X. Hu, "Unique Huygens-Fresnel electromagnetic transportation of chiral Dirac wavelet in a topological photonic crystal," Nat. Commun. **14**, 3040 (2023).
[24]D. Ge, H. Chen, Z. Hu, J. Shi, and L. Zhang, "A new one-dimensional photonic crystal magnetic sensor based on magnetic fluid film with excellent sensing ability and figure of merit," J. Magn. Magn. Mater. **545**, 168753 (2022).
[25]Z. Baraket, J. Zaghdoudi, and M. Kanzari, "Investigation of the 1D symmetrical linear graded superconductor-dielectric photonic crystals and its potential applications as an optimized low-temperature sensors," Opt. Mater. **64**, 147–151 (2017).
[26]Z. A. Zaky, A. M. Ahmed, A. S. Shalaby, and A. H. Aly, "Refractive index gas sensor based on the Tamm state in a one-dimensional photonic crystal: Theoretical optimization," Sci. Rep. **10**, 9736 (2020).
[27]L. Stern, A. Naiman, G. Keinan, N. Mazurski, M. Grajower, and U. Levy, "Ultra-precise optical to radio frequency based chip-scale refractive index and temperature sensor," Optica **4**, 1–7 (2017).
[28]B. F. Wan, Y. Xu, Z. W. Zhou, D. Zhang, and H. F. Zhang, "Theoretical investigation of a sensor based on one-dimensional photonic crystals to measure four physical quantities," IEEE Sens. J. **21**, 2846–2853 (2021).
[29]X. Lu, A. McClung, and K. Srinivasan, "High-*Q* slow light and its localization in a photonic crystal microring," Nat. Photonics **16**, 66–71 (2022).
[30]Y. Trabelsi, N. Ben Ali, F. Segovia-Chaves, and H. V. Posada, "Photonic band gap properties of one-dimensional photonic quasicrystals containing Nematic liquid crystal," Results Phys. **19**, 103600 (2020).
[31]I. Dierking, M. Ravnik, E. Lark, J. Healey, G. P. Alexander, and J. M. Yeomans, "Anisotropy in the annihilation dynamics of umbilic defects in nematic liquid crystal," Phys. Rev. E **85**, 021703 (2012).
[32]L. Qi, Z. Yang, F. Lan, X. Gao, and Z. Shi, "Properties of obliquely incident electromagnetic wave in one-dimensional magnetized plasma photonic crystals," Phys. Plasmas **17**, 021703 (2010).
[33]S. Guo, C. Hu, and H. Zhang, "Ultra-wide unidirectional infrared absorber based on 1D gyromagnetic photonic crystals concatenated with general Fibonacci quasi-periodic structure in transverse magnetization," J. Opt. **22**, 105101 (2020).
[34]L. Lewin, "The electrical constants of a material loaded with spherical particles," J. Inst. Electr. Eng., Part III **94**, 65–68 (1947).
[35]L. Xuan, X. Kong, J. Wu, Y. He, and Z. Xu, "A smoothly-connected crescent transverse gradient coil design for 50mT MRI system," Appl. Magn. Reson. **52**, 649–660 (2021).
[36]S. Kumar, A. Bisht, G. Singh, K. Choudhary, K. K. Raina, and A. Amphawan, "Design of 1-bit and 2-bit magnitude comparators using electro-optic effect in Mach–Zehnder interferometers," Opt. Commun. **357**, 127–147 (2015).
[37]S. Kumar, A. Bisht, G. Singh, K. Choudhary, and D. Sharma, "Implementation of wavelength selector based on electro-optic effect in Mach–Zehnder interferometers for high speed communications," Opt. Commun. **350**, 108–118 (2015).
[38]S. Kumar, G. Singh, A. Bisht, S. Sharma, and A. Amphawan, "Proposed new approach to the design of universal logic gates using the electro-optic effect in Mach–Zehnder interferometers," Appl. Opt. **54**, 8479 (2015).
[39]M. S. Zakerhamidi and H. Rahimzadeh, "Order parameters and refractive indices of some cyano-benzoate nematic liquid crystal with high transition temperatures," J. Mol. Liq. **172**, 41–45 (2012).
[40]A. G. Mohamed, W. Sabra, A. Mehaney, A. H. Aly, and H. A. Elsayed, "Multiplication of photonic band gaps in one-dimensional photonic crystals by using hyperbolic metamaterial in IR range," Sci. Rep. **13**, 324 (2023).
[41]W. L. Bade, "Drude-model calculation of dispersion forces. I. General theory," J. Chem. Phys. **27**, 1280–1284 (1957).
[42]V. Yannopapas, A. Modinos, and N. Stefanou, "Scattering and absorption of light by periodic and nearly periodic metallodielectric structures," Opt. Quantum Electron. **34**, 227–234 (2002).
[43]A. G. Asuero, A. Sayago, and A. G. González, "The correlation coefficient: An overview," Crit. Rev. Anal. Chem. **36**, 41–59 (2006).
[44]B. F. Wan, Q.-Y. Wang, H.-M. Peng, H.-N. Ye, and H.-F. Zhang, "A late-model optical biochemical sensor based on OTS for methane gas and glucose solution concentration detection," IEEE Sens. J. **21**, 21465–21472 (2021).
[45]K. Wallace, G. Hardy, and E. Serabyn, "Deep and stable interferometric nulling of broadband light with implications for observing planets around nearby stars," Nature **406**, 700–702 (2000).
[46]R. Kerr, A. L. Kraus, and A. C. Rizzuto, "SPYGLASS. IV. New stellar survey of recent star formation within 1 kpc," Astrophys. J. **954**, 134 (2023).
[47]H. Nikaein, A. Sheikhi, and S. Gazor, "Target detection in passive radar sensors using least angle regression," IEEE Sens. J. **21**, 4533–4542 (2021).
[48]J. J. H. Wang, "Antennas for Global Navigation Satellite System (GNSS)," Proc. IEEE **100**, 2349–2355 (2012).
[49]G. Laurent, Y. Vyatkin, D. Antonets, M. Ri, Y. Qi, O. Saik, D. Shtokalo, M. J. L. de Hoon, H. Kawaji, M. Itoh, T. Lassmann, E. Arner, A. R. R. Forrest, E. Nicolas, T. A. McCaffrey, P. Carninci, Y. Hayashizaki, C. Wahlestedt, and P. Kapranov, "Functional annotation of the vlinc class of non-coding RNAs using systems biology approach," Nucl. Acids Res. **44**, 3233–3252 (2016).
[50]B. Trathnigg, "Determination of chemical composition of polymers by sec with coupled density and Ri detection. I. Polyethylene glycol and polypropylene glycol," J. Liq. Chromatogr. **13**, 1731–1743 (1990).
[51]R. Rahad, A. K. M. Rakib, M. A. Haque, S. S. Sharar, and R. H. Sagor, "Plasmonic refractive index sensing in the early diagnosis of diabetes, anemia, and cancer: An exploration of biological biomarkers," Results Phys. **49**, 106478 (2023).
[52]J. Zhang, S. Gong, X. Li, J. Liang, Z. L. Wang, and K. Ren, "A wind-driven poly (tetrafluoroethylene) electret and polylactide polymer-based hybrid nanogenerator for self-powered temperature detection system," Adv. Sustainable Syst. **5**, 2000192 (2020).
[53]Y.-P. Yang, K.-C. Lin, I.-C. Yang, K.-Y. Lee, Y.-J. Lin, W.-Y. Lee, and Y.-T. Tsai, "All-optical photonic crystal AND gate with multiple operating wavelengths," Opt. Commun. **297**, 165–168 (2013).
[54]B. Memarzadeh Isfahani, T. Ahamdi Tameh, N. Granpayeh, and A. Reza, "All-optical NOR gate based on nonlinear photonic crystal microring resonators," J. Opt. Soc. Am. B **26**, 1097 (2009).
[55]M. Y. Azab, M. Farhat, O. Hameed, and S. S. A. Obayya, "Multi-functional optical sensor based on plasmonic photonic liquid crystal fibers," Opt. Quantum Electron. **49**, 49 (2017).

[56]M. K. Khalaf, S. R. Tahhan, H. J. Taher, S. M. Ibrahim, and K. Ahmed, "Au-TiO_2 coated dielectric micro-channel based plasmonic refractive index sensor," Opt. Quantum Electron. **55**, 612 (2023).
[57]Y. T. Xiang, B. F. Wan, and H. F. Zhang, "Multiscale and multiple physical quantities sensor based on nonreciprocal evanescent wave in the one-dimensional photonic crystals," IEEE Sens. J. **21**, 19984–19992 (2021).
[58]Y. Liu, C. Zhao, Y. Zhang, G. Ma, X. Li, and Y. Zhao, "Electrically tunable optical fiber device based on hollow-core fiber infiltrated with liquid crystal," Sens. Actuators, A **318**, 112500 (2021).
[59]L. Zhe, Y. Hang, H. Wu *et al.*, "Self-phase modulation in integrated cadmium telluride polycrystalline waveguide," Opto-Electron. Eng. **50**(2), 220313 (2023).
[60]G. S. Deng, A. R. Guo, X. Q. Cheng *et al.*, "Dual-layer 3D terahertz metamaterial based multifunctional sensor," Opto-Electron. Eng. **51**(10), 240164 (2024).